



**Politecnico  
di Torino**

POLITECNICO DI TORINO

Master Degree Thesis in Electronic Engineering

**Design and Optimization of a Blue Laser  
Processing Head for Additive  
Manufacturing Applications**

**Supervisors**

Prof. Guido PERRONE

**Candidate**

Luca MAGGIO-TANASI

ACADEMIC YEAR 2022-2023



# Acknowledgements



## Abstract

Recent applications of Additive Manufacturing (AM) pose new challenges that are difficult to meet with the commonly used Infrared (IR) laser, but instead could be well addressed by blue lasers. Indeed, while high-power IR lasers have found extensive usage in materials processing, switching to blue lasers would improve the processing quality and efficiency of some materials that are finding increasing importance in industrial applications, such as copper, gold and aluminum, because of their higher absorption in the blue wavelengths than in the IR region. This also improves the energy consumption since blue laser diodes show a higher Wall Plug Efficiency (WPE) than IR fiber lasers.

The objective of the thesis is the design, fabrication and preliminary characterization of a processing head for blue light, specifically conceived to be installed on the prototype of an innovative, low-cost AM machine. The laser source can emit some hundreds of watts, obtained from the combination of multi-emitter diode modules. The new machine is intended for the manufacturing of small-volume parts utilizing both high-performance semi-crystalline engineering thermoplastics and metals that are currently challenging to process using lasers.

The processing head consists of an optical system based on spherical lenses and does not make use of galvo mirrors: the selection of this type of lenses as the preferred optics to be installed in the processing head was motivated by the need to maintain low construction costs.

As a preliminary design step a custom code for the analysis of a lens system using Gaussian beams, ray tracing and the ray transfer matrix approach was developed and validated against a commercial software. This has allowed to determine the optimal sequence of lenses and focal lengths required to manipulate the beam, so as to yield the desired characteristics in terms of focused spot shape and power density.

Then, thermal simulations were performed using a finite element analysis software (COMSOL) to evaluate the heating of the optics and to determine the optimal lens material. A Gaussian beam with power characteristics similar to those of the employed laser source was simulated to propagate through the optical system devised in the initial design phase. The predictions were validated with some lab experiments.

As a final phase of the design process, advanced ray tracing simulations were conducted using Zemax OpticStudio software to model a source comprised of a combination of multi-emitters. This source possessed beam characteristics that were closely akin to those of the commercial modules that will be employed in the construction of the final product. The use of OpticStudio facilitated the simulation of laser beams that exhibited more intricate field distributions than Gaussian ones. It also allowed for a more precise prediction of the intensity profile of the focused spot in the end product.

A lab prototype of the processing head was built and fully characterized, obtaining

results in good agreement with the theoretical predictions. These findings provide the basis for future developments, with the potential for achieving a modular and scalable in power system.

# Contents

Abstract . . . . .	i
<b>List of Figures</b>	v
<b>1 Introduction</b>	1
1.1 Additive manufacturing . . . . .	1
1.1.1 Market trends . . . . .	1
1.2 Laser source . . . . .	4
1.2.1 Laser parameters affecting AM . . . . .	4
1.3 Thesis Overview . . . . .	7
<b>2 Theoretical background</b>	9
2.1 Gaussian beams . . . . .	9
2.2 Real Gaussian Beams . . . . .	11
2.3 Lenses . . . . .	13
<b>3 Simulations on gaussian beams</b>	17
3.1 Complex Beam Parameter and Geometrical Optics . . . . .	17
3.2 Five rays technique . . . . .	18
3.3 Definition of the optical system . . . . .	20
3.3.1 Galilean beam expander . . . . .	21
3.3.2 Design of the focusing length . . . . .	24
<b>4 Thermal analysis</b>	27
4.1 Simulation of the Infrared setup . . . . .	28
4.2 Experimental measurement on the Infrared setup . . . . .	30
4.3 Simulation of the Blue setup . . . . .	31
4.4 Thermally induced focal shift analysis . . . . .	33
<b>5 Advanced ray tracing</b>	35
5.1 Source simulation . . . . .	35
5.2 Simulation of the optical system . . . . .	38
5.3 Analysis of the simulation results . . . . .	39

<b>6</b>	<b>Experimental setup</b>	41
6.1	Beam expander assembly and collimation . . . . .	42
6.2	Assembly of the focusing lens . . . . .	44
6.3	Measurement of the spot size . . . . .	46
6.4	Measurement of the divergence . . . . .	47
6.5	Measurement of the thermally induced focal shift . . . . .	48
<b>7</b>	<b>Conclusions</b>	49
7.1	Results achieved . . . . .	49
7.2	Outlook . . . . .	50
	<b>Bibliography</b>	53

# List of Figures

1.1	Global laser technology market revenue analysis and forecast. . . . .	2
1.2	Global Laser Technology Market by application 2021 (USD Million). . . .	2
1.3	Metal Additive Manufacturing Market share by type. . . . .	3
1.4	Global Laser Technology Market by laser type 2021 (% share). . . . .	3
1.5	Absorption characteristics of various metals vs wavelength. . . . .	5
2.1	Gaussian beam intensity and amplitude distribution. . . . .	10
2.2	Positive and negative lenses. . . . .	13
2.3	Rays diagram of a lens. . . . .	14
2.4	Correct (left) and wrong (right) orientations of a plano-convex aiming at minimizing the spherical aberrations. . . . .	15
3.1	Example of the five rays trajectories for the Gaussian beam ray equivalent model of a laser source. . . . .	19
3.2	Ray tracing scheme of the configuration with one single focusing lens. . .	21
3.3	Galilean beam expander. . . . .	22
3.4	Ray tracing scheme of the collimation through the beam expander. . . .	23
3.5	Ray tracing scheme of the system with beam expander and focusing lens. .	24
4.1	COMSOL simulation setup. . . . .	28
4.2	Heating of the lens with 1 kW infrared radiation simulated in COMSOL. .	29
4.3	Heat map of the lens with 1 kW infrared radiation simulated in COMSOL. .	29
4.4	Experimental setup for temperature measurements on the infrared setup. .	30
4.5	Trend of the temperature detected on the center of lens by the FLIR thermal imaging camera. . . . .	31
4.6	Heating of the lens with 1 kW infrared radiation simulated in COMSOL. .	32
4.7	Heat map of the lens with 120 W blue radiation simulated in COMSOL. .	32
5.1	Output characteristic of the multi-emitters modules. . . . .	35
5.2	Graphical explanation of the Astigmatism parameter from OpticStudio's help guide. . . . .	36
5.3	Spot diagram of a simulated source. . . . .	37
5.4	Spot diagram of the superposition of two simulated sources spectrally combined. . . . .	37

5.5	Lenses sequence in OpticStudio 3D Non-Sequential Component view with traced rays. . . . .	38
5.6	Spot diagram of the collimated beam exiting the beam expander. . . . .	39
5.7	Final spot detected at the focus of the focusing lens. . . . .	40
6.1	Example of Thorlabs' cage system. . . . .	41
6.2	Thorlabs 3-axis kinematic lens mounts. . . . .	42
6.3	Multi-emitter module arranged for air output. . . . .	43
6.4	Beam expander assembled with cage system. . . . .	43
6.5	Processing head fully assembled with cage system. . . . .	44
6.6	CMOS camera used for the spot measurements (Thorlabs DCC3260C). . . . .	45
6.7	System used to detect the focused spot. . . . .	45
6.8	Image of the focused spot captured with Thorlabs CMOS camera. . . . .	46
6.9	Image of the spot captured at 10 mm away from the focal point with Thorlabs CMOS camera. . . . .	47
7.1	Spot of the collimated beam obtained from the spatial combination of two spectral combined source (four modules in total). . . . .	51
7.2	Schematic of an axicon lens' working principle. . . . .	51

# Chapter 1

## Introduction

### 1.1 Additive manufacturing

Additive manufacturing, especially laser additive manufacturing (LAM), is a novel manufacturing technique for material processing which owns advantages of rapid prototyping, customization, high material utilization, and the ability to form complicated structures. It has been accurately defined as a process of joining materials to make objects from 3D model data [1]. It consists of layer-by-layer forming according to geometric model generated from computer aided design (CAD) software that allows fabrication of complex, custom metal or alloy products which is almost impossible to achieve by a conventional processing (e. g. subtractive manufacturing methodologies, forging, casting); moreover AM technology minimizes lead time by reason of no need of traditional process tools and procedures resulting in less material waste without subsequent part assembly process. AM technologies are already exploited by many applications in the field of automotive, aerospace, architecture, biomedical, electronics industries, based on the fact that a variety of materials including metals, ceramics, polymers and composite materials can be processed.

According to the difference of heat sources, AM technology for metal can be roughly classified into three types: wire and arc additive manufacturing (WAAM), electron beam additive manufacturing (EBAM) and laser additive manufacturing (LAM). WAAM is mainly suitable for rapid prototyping of large size components, while EBAM and LAM are both applicable for small parts. LAM is the most promising AM technology for metal currently.

#### 1.1.1 Market trends

Recent years have witnessed a rapid growth of the laser market. As reported in Figure 1.1 [2], the Global Laser Technology Market Size accounted for USD 11.579 Million and is estimated to achieve a market size of USD 24,171 Million by 2030 growing at a CAGR of 8.7% from 2022 to 2030 [3].

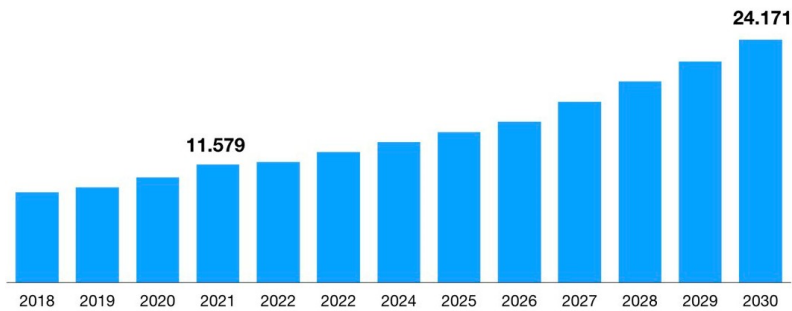


Figure 1.1: Global laser technology market revenue analysis and forecast.

By application, the laser processing segment has accounted 60% market share in 2021 as depicted in Figure 1.2.

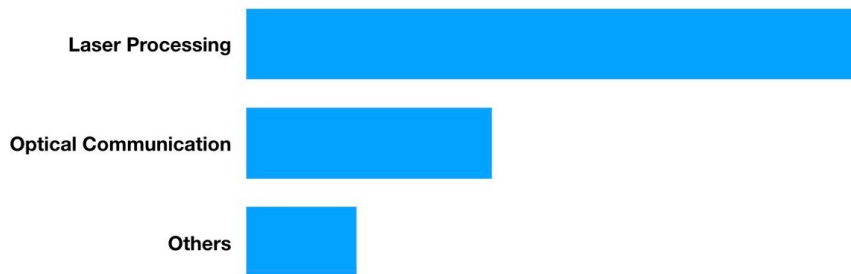


Figure 1.2: Global Laser Technology Market by application 2021 (USD Million).

Lasers have been the increasingly important core of additive manufacturing, with selective laser melting (SLM) becoming the fastest-growing Segment in the Metal Additive Manufacturing Market, as reported in Figure 1.3. SLM was valued at USD 1,395.20 million in 2017 and continued to grow until 2021. Due to the easy production of finite parts its demand is forecast to increase which, in turn, will boost the growth of the market during the next five years.

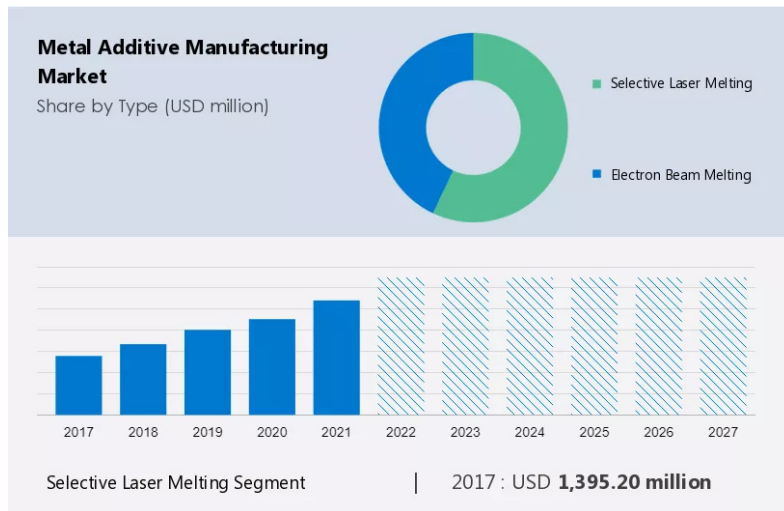


Figure 1.3: Metal Additive Manufacturing Market share by type.

In terms of laser type, Figure 1.4 shows that the solid-state laser segment will dominate the market during the forecast period due to the small region of the emission spectra used in the absorption process which leads to good absorption capability and great efficiency. Moreover, diode-pumped solid-state laser has the advantage of being extremely compact, light in weight and small in size.

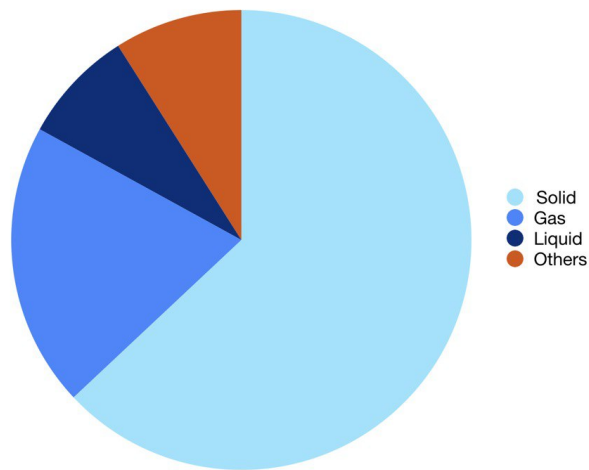


Figure 1.4: Global Laser Technology Market by laser type 2021 (% share).

## 1.2 Laser source

Carbon dioxide (CO<sub>2</sub>) lasers are one of the earliest gas discharge lasers and are the workhorse of precision manufacturing with 10.6 μm being the most widely used wavelength in AM. The disadvantages of this type of lasers are non-stable output power due to thermal expansion and contraction of the laser structure, their low Wall-Plug Efficiency (WPE) (5-15%) and their large size to guarantee air-tightness and dust-free operation. Moreover, optics with optimal mechanical properties at the working wavelength have poor availability.

As regards additive manufacturing, fiber lasers (FL) are one of the most widely used sources. A FL is a laser in which the active gain medium is a rare-earth doped optical fiber. The most suitable fiber dopant for high power generation is the Yb because of its high quantum efficiency (~94%) and for this reason, Yb-fiber lasers are widely used in material processing and in particular are specifically employed in AM. This type of laser produces near-infrared output in 1030 nm-1080 nm range. As opposed to CO<sub>2</sub>, it shows off an higher WPE approximately between 30% and 40%. Furthermore, it has excellent beam quality, robustness against environmental disturbances, and system compactness.

For what concerns WPE in particular, Diode Lasers (DLs) are some of the most efficient devices in converting electrical into optical energy, working at wall plug efficiencies up to 50-80%. So far, High-power DLs are packaged in multi-emitter modules used for laser pumping of solid-state lasers among other applications. Although their beam quality is not as good as fiber lasers, DLs are increasingly used for direct material processing, as they have demonstrated improved performance in terms of more uniform melt and heating zones, greater consistency and repeatability compared to CO<sub>2</sub> lasers. [4].

### 1.2.1 Laser parameters affecting AM

Lasers can be specified with several parameters such as average power, power stability, central wavelength, spectral bandwidth, beam diameter, beam quality, pulse energy, pulse duration and repetition rate.

The properties of the laser beam produced, included the wavelength of emission, depend on the gain medium and a particular range of wavelengths of choice could be convenient to process specific materials rather than others. The operating wavelength of the laser is the most important parameter to be considered in additive manufacturing because different materials interact with different laser wavelengths.

Figure 1.5 shows the absorptivity of various materials. In laser-based additive manufacturing, a high material absorption at the laser wavelength is desired since the target material should efficiently interact with the incident laser light; high absorptivity generally leads to high manufacturing throughput.

For metal powders, the shorter the wavelength, the better the light absorptivity,

therefore BLs is better absorbed than IR or CO<sub>2</sub> lasers. The NIR laser is the current dominant laser, but the reflectivity of aluminum, copper and other non-ferrous metals at this wavelength are more than 95% leading to extremely poor energy utilization. In order to obtain a greater energy transfer, the NIR laser needs a higher output power. However, it is more likely to give rise to defects such as pores and cracks, and the forming quality of the workpiece is inferior. Therefore, overcoming the high laser reflectivity has become a key issue in laser metal processing. As reported in Figure 1.5 blue lasers is the best choice when dealing with metals due to the efficient absorption of those wavelength.

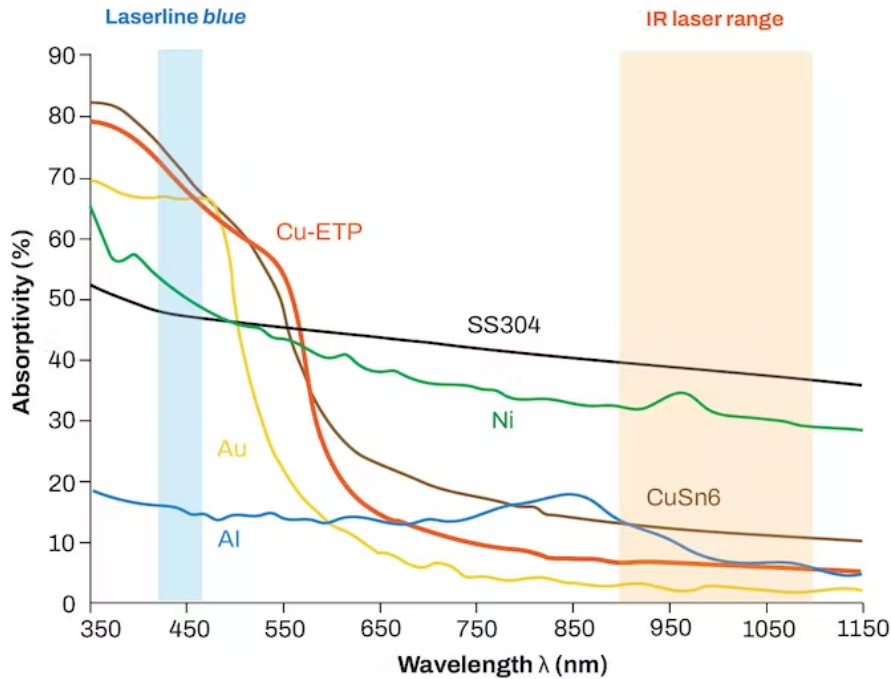


Figure 1.5: Absorption characteristics of various metals vs wavelength.

Moreover, blue laser heads feature much higher power density than CO<sub>2</sub> and NIR lasers despite the lower total power. In fact, the state of the art for blue single emitter is 10 W, while IR single emitter can reach up to 30 W [5]. The reason behind the lower achievable power of GaN-based laser diode is the low power conversion efficiency ( $\eta_{PCE}$ ). The most efficient laser diodes today are based on GaAs and some reach  $\eta_{PCE} > 70\%$  in continuous wave (CW) operation at room temperature while GaN-based laser diode can reach up to 40%. Large series resistance (one order of magnitude greater than GaAs-lasers'), increasing Auger recombination with high powers and enhanced free-carrier absorption are the main limiting factors [6].

At a given wavelength, beam quality and focused spot size are the laser parameters which should be considered to improve the manufacturing precision. To define beam

quality, Beam Parameter Product (BPP) is the product of the beam waist and the half-angle of beam divergence with the units of  $\text{mm} \cdot \text{mrad}$  (millimeters times milliradians). Because the low BPP means Gaussian beam profile with higher energy confinement, BPP is closely correlated to the power density and affects the manufacturing resolution. The factor depends on the gain medium, pumping source, resonator structure, and operating wavelength. The latter, in particular, determines the lower limit of BPP, which is  $\frac{\lambda}{\pi}$ , defined as the diffraction-limit. The degree of variation of a laser beam from an ideal Gaussian one is represented by the  $M^2$  factor.

As regards the injection of driving current in laser powder bed fusion process (L-PBF), CW or pulsed wave (PW) operation can be distinguished. During the L-PBF, the metallic material undergoes a complex cycle of heating and cooling. Previous research has indicated that this thermal history can result in a range of issues with the deposited material, including defects such as lack of fusion and porosity, accumulation of residual stresses and microstructural inhomogeneity that can lead to anisotropy in the mechanical properties. Melting and rapid solidification during the manufacturing process typically generate residual stresses, which can be reduced by preheating the build plate during manufacturing or by conducting post-thermal treatments such as stress relief and hot isostatic pressing. An additional processing strategy to reduce these imperfections could be the use of PW. There are several advantages to using pulsed lasers in additive manufacturing, as opposed to CW lasers. Pulsed lasers can deliver much higher peak powers than CW lasers, which can be beneficial for tasks such as breaking up and removing material. This higher peak power can also lead to better material properties, such as increased density, smoother surface finish, and improved mechanical properties [7]. It also widens the range of materials that can be processed, including metals, ceramics, polymers, and composites overcoming the thermal conductivity of certain materials, allowing them to be melted and processed. PW lasers provide increased control over the amount of heat being applied to the material, which can be important for preventing thermal damage to the workpiece and achieving optimal microstructural properties. In particular, Crystal structure of the as-built pulsed L-PBF material is less oriented and less columnar than continuous L-PBF resulting in stronger and stiffer pieces. Moreover it can be used to achieve very fine feature sizes and high resolution, which is important for creating complex geometries and detailed structures. The specific advantages will depend on the application and the specific properties of the material being processed. It has not been thoroughly examined and any work done to date has been focused on aluminium and titanium alloys. Hence, there is a gap in the state-of-the-art to see the effect of a pulsed laser heat source on the microstructure and mechanical properties of different materials and the possibility of achieving higher homogeneity in grain structure due to higher cooling rates.

## 1.3 Thesis Overview

Based on the introduced parameters in the previous section, a blue laser source has been designed for LAM and in particular for laser powder bed fusion of PEEK and metals.

The goal is to maximize the absorption in order to improve the efficiency avoiding imperfections due to excessive power density not properly absorbed by the powder. In order to do so, a blue laser system is been developed, aiming at reducing costs and providing a compact solution. Multi-emitters instead of fiber lasers have been selected to assure lower costs to detriment of beam quality. More in details the target for what concerns the spot size is set to 150  $\mu\text{m}$  and the total power of the laser source settles down around 100 W.

The system developed consists of a unique block which incorporate the combined source and the processing head, mounted on an AM machine and relocated through a system of mechanical slides.

The source is modular, the building block is made of multi-emitters spectrally combined. The choice of such approach is motivated by the necessity to adapt the total power of the source to process different materials in order to minimize costs according to the number of modules used. In this way there is no need of reconfiguration of the entire system when there is necessity to scale power to process metals instead of plastic polymers. Coarse spectral combination is employed. In order to avoid overlapping of spectrum, an early step of stabilization is added to tune the emission at different wavelengths. The proposed scheme's only drawback is that the combined beam's emission spectrum contains the spectral contribution of the single emitters, resulting in decreased laser spectral brightness. However, for material processing applications, where spatial brightness is more important than spectral brightness, the proposed architecture has proven to be a valid alternative to other laser solutions.

For what concern the processing head, the presence of mechanical slides which move the source the use of a Galvo Mirror System is not fundamental and fixed optics have been preferred in order to contain costs.

In the present work, the focus is on the processing head and the solution adopted to manipulate the beam produced by the spectral combination.

The preliminary laboratory tests have been performed on 30 W multi-emitter blue modules instead of the 60 W modules planned to be inserted in the final prototype. However, considering that the only difference between the 30 W and the 60 W modules is a polarization combination stage, the dimension of the spot and its evolution along the optical path is invariant.

Commercial fused silica lenses have been used for the construction of the benchtop prototype.

An introduction to Gaussian beams and lenses is presented in chapter 2 to clarify the theoretical aspects besides the performed design considerations.

In chapter 3 preliminary calculations on real Gaussian beams have been carried out in order to individuate the optimal optical path to achieve the required specifications.

Several considerations about the heating of the optical elements and its consequences are present in chapter 4.

Then, chapter 5 deals with an advanced ray tracing activity carried out in order to obtain precise information about the spot shape and the intensity profile of the beam focused on the target plane.

To conclude, in chapter 6, all the results coming from the experimental activity are analyzed and compared with the specification to validate all the simulations performed in the design phase.

## Chapter 2

# Theoretical background

### 2.1 Gaussian beams

Gaussian field distributions are important in the study of light beam propagation because they offer the advantages of analytical simplicity but also possess finite energy. This makes them a physically realistic solution that closely approximates actual beams emitted by lasers.

$$\left(\nabla^2 + k^2\right) \underline{E}(r) = 0. \quad (2.1)$$

Gaussian beams are derived from the Helmholtz equation, which represent the wave equation in a time independent form. Although plane waves are a useful theoretical concept, they cannot be physically realized because they have constant electric and magnetic field magnitudes that extend to infinity. Consequently, they would carry an infinite amount of energy, which is not physically realistic.

Gaussian beams, on the other hand, are a more realistic solution for describing actual beams emitted by lasers. They are derived from the paraxial Helmholtz equation, which is an approximation obtained by looking for a solution in the form of an envelope. This equation describes the propagation of light waves in the direction of  $z$ , and can be expressed in terms of the scalar wave equation.

$$E(r, z) = u(r, z) \exp[-jkz] \quad (2.2)$$

Substituting Equation 2.2 in the scalar version of Equation 2.1, expanding the Laplace operator, and neglecting the second order partial derivative along  $z$  given the slow dependency of  $E_0$  with  $z$ , the paraxial Helmholtz equation (Equation 2.3) is obtained:

$$\left(\frac{\partial^2}{\partial x^2} + \frac{\partial^2}{\partial y^2} - 2jk \frac{\partial}{\partial z}\right) u(x, y, z) = 0 \quad (2.3)$$

The solutions of the approximated Helmholtz equation are parabolic waves known as

Gaussian beams, which are described by:

$$E(x, y, z) = E_0 \frac{w_0}{w(z)} \exp\left(-\frac{r^2}{w^2(z)}\right) \exp\left[-j\left(kz - \frac{kr^2}{2R(z)} - \phi(z)\right)\right] \quad (2.4)$$

The amplitude of a Gaussian beam is described by the first exponential, which is a function of the peak field amplitude  $E_0$  and the decay factor  $w_0/w(z)$ . These parameters determine how the field amplitude changes with respect to the spatial coordinate  $r$  and the propagation direction  $z$ . The subsequent exponentials describe the longitudinal and radial phase factors, which determine the changes in beam phase along the optical axis  $z$  and the shape of the wavefront.

Gaussian beams are unique in that they exhibit wavefront behavior similar to that of plane waves at the point of minimum spot size. As the beam propagates away from this point, the wavefronts transform into spherical shapes (Figure 2.1). Thus, the amplitude and phase factors of the Gaussian beam equation provide a comprehensive description of the spatial and temporal properties of the beam, including its spot size, divergence, and polarization state.

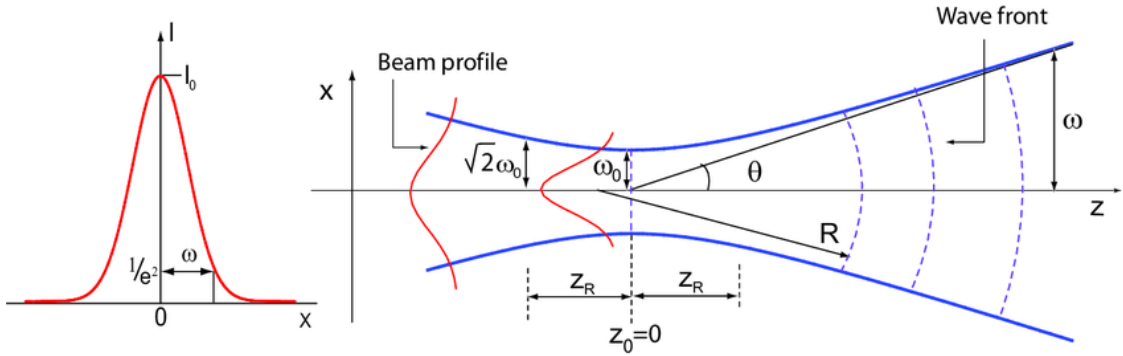


Figure 2.1: Gaussian beam intensity and amplitude distribution.

Referring at Equation 2.4, the fundamental parameters are:

- the beam waist  $w_0$ , defined as the smallest point of the beam radius  $w(z)$ . It represents the minimum section of the spot size.
- the beam radius  $w(z)$ , related to the beam waist as:

$$w(z) = w_0 \cdot \sqrt{\left[1 + \left(\frac{z}{z_R}\right)^2\right]} \quad (2.5)$$

- the Rayleigh range, which is a crucial parameter in Gaussian beam analysis, is the distance along the  $z$ -axis from the waist position to the location where the cross-sectional area of the beam has doubled. In other words, it is the distance over which

the beam undergoes significant changes in its spatial profile.

$$z_R = \frac{\pi n w_0^2}{\lambda_0} \quad (2.6)$$

- the beam radius of curvature  $R(z)$ , which characterizes the wavefront of the beam along the z-direction. It describes the curvature of the beam's wavefront and can be calculated using Equation 2.7:

$$R(z) = w_0^2 \left[ 1 + \left( \frac{z}{z_R} \right)^2 \right] \quad (2.7)$$

- the divergence angle  $\theta$ , a parameter that characterizes the spread of a Gaussian beam in the far field. It is defined as half the angle between the optical axis and the cone-shaped beam curve and can be calculated using the formula:

$$\theta = \frac{\lambda_0}{\pi n w_0} \quad (2.8)$$

- The Guoy phase  $\phi$ , a correction factor that accounts for the Gaussian phase shift acquired by a beam as it passes through the focus. It represents the phase difference between the wavefronts of the beam and a reference plane wave at the same location.

$$\phi = \arctan \left( \frac{z}{z_R} \right) \quad (2.9)$$

## 2.2 Real Gaussian Beams

The fundamental mode of ideal gaussian beams is the  $TEM_{00}$ , it exhibits several characteristics which are highly desirable in any laser system. In particular it has maximal intensity on the optical axis and low divergence, making the optical power concentrated in the center of a thin ray of light that does not widen, and it is diffraction-limited so, for a specific wavelength, the focused spot is the smallest achievable.

However, those just mentioned are features which cannot be physically implemented in real laser sources.

A laser beam quality indicator, largely used in high power applications is the BPP. It is defined as the product between the beam waist radius  $w_0$  measured in near field and the beam divergence half angle  $\theta$  measured in far field and its units of measurement are mm·mrad.

$$BPP = w_0 \cdot \theta \quad (2.10)$$

The smallest possible BPP value is the one referred to an ideal gaussian beam and depends on the wavelength as reported in Equation 2.11.

$$BPP_{\text{ideal}} = \frac{\lambda}{\pi} \quad (2.11)$$

In addition to BPP,  $M^2$  is another parameter commonly used to compare laser sources. This quantity is preferable to BPP as it does not depend on the wavelength and it is dimensionless being defined as:

$$M^2 = \frac{BPP}{BPP_{\text{ideal}}} \quad (2.12)$$

The best result possible for a laser beam is  $M^2 = 1$  and as this value increases the quality of the laser source decreases.

The factor  $M^2$  affects the fundamental parameters which characterize the gaussian beam:

- the beam radius becomes larger with a worsening of the intensity profile:

$$w_{\text{real}}(z) = \sqrt{M^2} w_{0\text{ideal}} \cdot \sqrt{\left[ 1 + \left( \frac{\lambda z}{\pi w_{0\text{ideal}}^2} \right)^2 \right]} \quad (2.13)$$

- the beam divergence half-angle becomes larger (Equation 2.14) and consequently the Rayleigh range is reduced (Equation 2.15):

$$\theta_{\text{real}} = \frac{M^2 \lambda}{\pi w_{0\text{real}}} \quad (2.14)$$

$$z_{\text{Rreal}} = \frac{\pi n w_{0\text{real}}^2}{M^2 \lambda_0} \quad (2.15)$$

## 2.3 Lenses

A lens can be defined as an optical device made of transparent material, typically a dielectric like fused silica, that alters the direction of light rays passing through it in a specific manner, utilizing the principle of Snell’s law of refraction (Equation 2.16) [8].

$$n_1 \sin \theta_1 = n_2 \sin \theta_2 \quad (2.16)$$

This modification of the beam’s propagation can result in the convergence of rays towards a particular point in the case of positive lenses, or their divergence as if emanating from a specific point in the case of negative lenses, thus enabling the creation of real or virtual images of a source. In essence, lenses are optical components that utilize the phenomenon of refraction to alter the path of light rays and produce images.

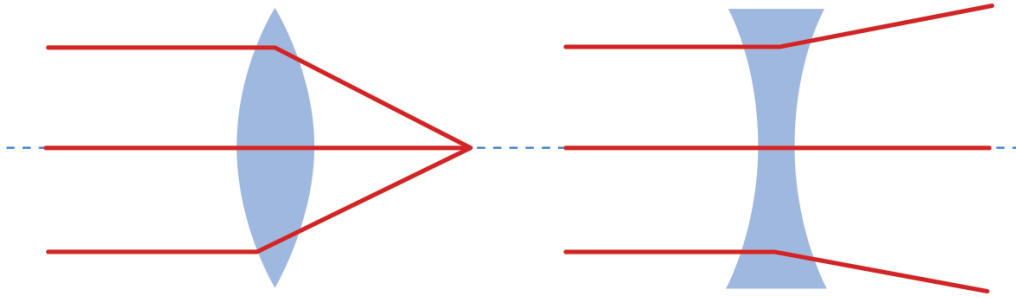


Figure 2.2: Positive and negative lenses.

Lenses can be categorized into two types based on their thickness: thin lenses, where the center thickness is much smaller than the radius of curvature of the surfaces, and thick lenses, where the thickness is not negligible compared to the radius of curvature.

Several shapes of positive and negative lenses are available, but for the realization of the processing head, only two types are used to perform the necessary beam manipulations (Figure 2.2):

- Plano-Convex Positive Lenses
  
- Plano-Concave Negative Lenses

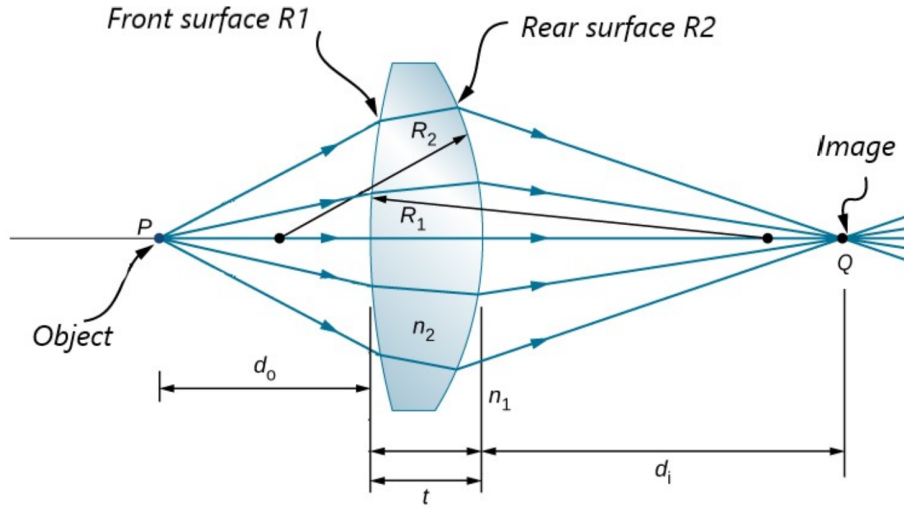


Figure 2.3: Rays diagram of a lens.

The parameters of the lenses that are relevant for the design and have been taken into consideration are:

- $D$ , the diameter of the lens.
- $R$ , the radius of curvature of the lens, intended as the directed distance from the vertex of a surface to the center of curvature (Figure 2.3).
- EFL, the Effective Focal Length, which is the distance between the principal plane of the lens and the imaging plane.
- BFL, the Back Focal Length, which is the distance from the last surface of the lens to the image plane.
- NA, the Numerical Aperture, a crucial parameter in lens design which indicates the amount of radiation that the lens can collect. NA is determined by the refractive index ( $n$ ) of the medium between the source and the lens and the half acceptance angle ( $\alpha$ ). Alternatively, NA can be expressed in terms of the focal length ( $f$ ) and the diameter ( $D$ ) of the lens.

$$NA = n \sin \alpha = n \sin \left[ \arctan \left( \frac{D}{2f} \right) \right] \simeq \frac{D}{2f} \quad (2.17)$$

Ideal lenses are characterized by their ability to produce images that are exact replicas of the imaged object, with collimated light focused to a spot size that is only limited by diffraction. Conversely, real lenses deviate from perfection and introduce optical aberrations that impair their ability to form high-quality images, collimate beams, or focus them tightly.

The main type of monochromatic aberrations which affects the described application is the spherical aberration and it refers to the departure of a wavefront from its perfect spherical shape, resulting in a bright central spot surrounded by a faint halo. In other words, when using spherical lenses, rays that are parallel to the optical axis but are incident at varying distances from it fail to converge at a single point.

Spherical aberrations depends on lens shape and orientation and can be minimized working on the arrangement of the optical system. When it comes to focusing parallel rays of light onto a single point, plano-convex lenses are the preferred option. These lenses feature a curved surface on one side and a flat surface on the other. To achieve optimal performance, it is crucial to orient the curved surface of the lens towards the collimated beam (Figure 2.4).

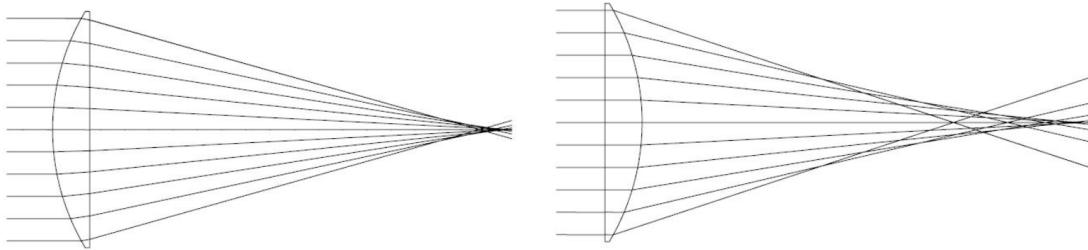


Figure 2.4: Correct (left) and wrong (right) orientations of a plano-convex aiming at minimizing the spherical aberrations.



## Chapter 3

# Simulations on gaussian beams

The initial step in designing the optical system that constitutes the processing head was to simulate the propagation of the beam exiting the source through a sequence of lenses. The simulation was carried out using a Matlab script based on Geometrical Optics (GO), Ray Transfer Matrix (RTM) and the Five rays technique.

### 3.1 Complex Beam Parameter and Geometrical Optics

It is possible to fully characterize Gaussian beams using a single complex beam parameter, typically denoted as  $q$ . This parameter can be defined in a manner that the phase and amplitude of the beam can be obtained from the real and imaginary components of its reciprocal  $1/q$ , respectively. The  $q$  parameter for a particular section at position  $z$  can be expressed as follows:

$$q(z) = z - j\frac{k}{2}w_0^2 = z + jz_R \quad (3.1)$$

Expressing the beam in terms of  $q$  offers the benefit of simplifying the calculation of  $q$ 's transformation through an optical system using GO and RTM.

GO is a branch of optics that approximates the behavior of light as rays that travel in straight lines and interact with optical components such as lenses and mirrors. It is based on the assumption that the wavelength of light is much smaller than the size of the optical components.

The RTM is a mathematical tool used in GO to describe the propagation of light through an optical system. It represents the transformation of a ray's position and angle as it passes through the system, allowing for the calculation of the location and properties of the image formed by the system. It is a matrix that relates the input and output coordinates and angles of a light ray passing through an optical element, taking into account the effects of refraction, reflection and other optical phenomena (Equation 3.2). The RTM can be used to design and analyze optical systems and to optimize their

performance.

$$\begin{bmatrix} r' \\ \theta' \end{bmatrix} = \begin{bmatrix} A & B \\ C & D \end{bmatrix} \begin{bmatrix} r \\ \theta \end{bmatrix} \quad (3.2)$$

The complex beam parameter for a beam that traverses an optical component described by a RTM is given by:

$$q_{\text{out}} = \frac{Aq_{\text{in}} + B}{Cq_{\text{in}} + D} \quad (3.3)$$

A thin lens with a focal length  $f$  can be modelled in GO with a RTM of the type:

$$\begin{bmatrix} 1 & 0 \\ -\frac{1}{f} & 0 \end{bmatrix} \quad (3.4)$$

The implementation of the lens class in the Matlab-based simulator facilitates the specification of a list of lenses with their corresponding parameters, such as diameter, focal length, position (along the z-axis with coordinates [x, y, z]) and optionally, the radii of curvature of the surfaces. This is accomplished by providing the relevant information in a .csv file.

## 3.2 Five rays technique

The Gaussian beam ray-equivalent method, also referred to as the five rays technique, is a modeling approach utilized to analyze Gaussian beams propagating within the paraxial approximation.

The technique involves tracing five paraxial rays, symmetrically distributed around the beam axis, as they propagate through optical components like lenses and mirrors.

These rays are utilized to determine a ray equivalent to the Gaussian beam, enabling the calculation of beam parameters, such as the beam waist and the propagation direction. This technique assumes that the Gaussian beam can be approximated by a bundle of paraxial rays that travel in a straight line, passing through the same point in the beam waist.

While this method is not suitable for modeling non-ideal behavior in terms of aberrations, it is appropriate for fitting non-Gaussian beams with  $M^2 > 1$ .

The five rays considered in the application of this technique are (Figure 3.1):

- Chief ray: is a ray of light that passes through the center of the entrance pupil of an optical system and it coincides with the optical axis. It determines the position of the image formed by the system.
- Waist rays: two rays which propagate parallel to the chief ray defining the beam waist size.
- Divergence rays: two rays that originate from the same point of the chief ray and propagate according to the divergence  $\theta$ .

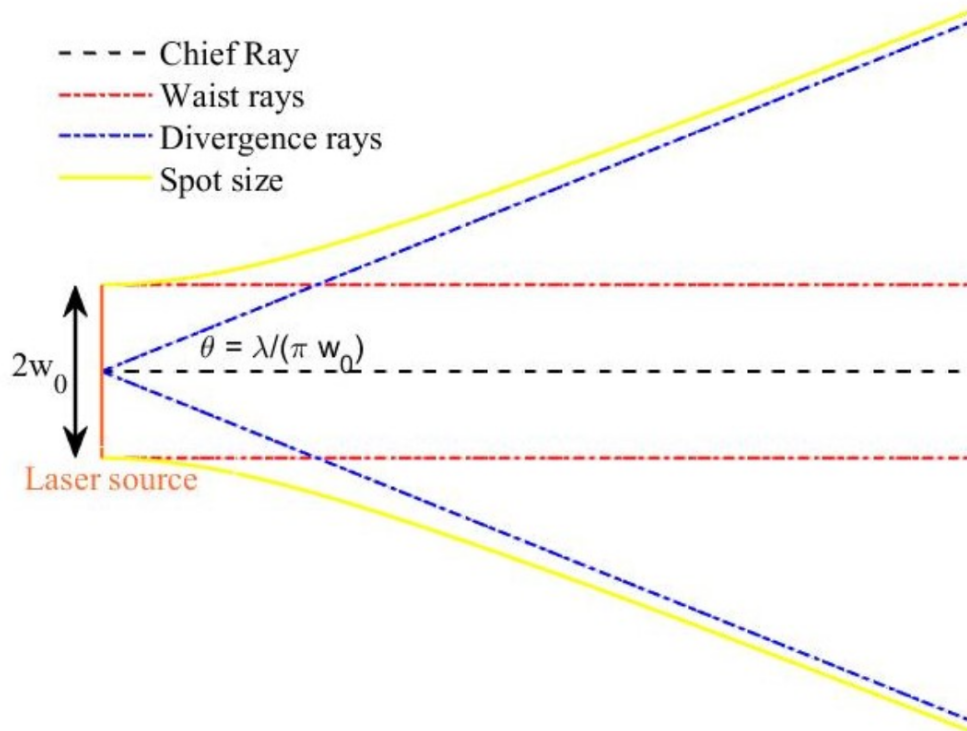


Figure 3.1: Example of the five rays trajectories for the Gaussian beam ray equivalent model of a laser source.

One benefit of utilizing the Five Rays Technique for beam propagation analysis is the ability to employ RTM and break down the analysis by examining each distinct ray type, thereby gaining insights into the evolution of the beam's parameters.

Indeed, this has made it possible to generate a detailed .txt format report file that includes essential information on the final spot, such as the beam waist, divergence and peak intensity. Additionally, a .png format file is produced, depicting the beam's evolution through the designated lens system.

### 3.3 Definition of the optical system

To design the required lens sequence for manipulating the beam, it is crucial to comprehend the properties of the employed laser source and the desired final spot specifications. The source consists of two commercial blue laser modules with an optical power of 60 W spectrally combined.

The primary advantage of spectral combining is to preserve the beam quality of the utilized sources, resulting in a more powerful beam while maintaining collimated beam dimensions similar to those of a single multi-emitter module. For this reason, the source utilized in the simulations was modeled based on the output characteristics declared in the datasheet of a single multi-emitter module.

As the result of combining the polarization of two ten CoC benches, spatially combined in turn, the beam produced by the multi-emitter modules deviates significantly from a beam with a Gaussian intensity profile. However, since this is a preliminary simulation, the source has been simulated as a collimated real astigmatic Gaussian beam with the following characteristics:

- Beam waist of 2.15 mm on the Slow Axis (SA) and 3.1 mm on the Fast Axis (FA).
- Residual divergence of 1.87 mrad on the SA and 1.93 mrad on the FA.
- The  $M^2$  is computed by the Matlab simulator starting from the values of beam waist and divergence specified in the .csv file describing the source. The values, in particular, are  $M_{SA}^2 = 14.20$  and  $M_{FA}^2 = 21.12$

The specifications required by the client regarding the obtained spot are set at a diameter between 100  $\mu\text{m}$  and 200  $\mu\text{m}$  at a distance of at least 120 mm from the exit window of the head. These requirements are dictated by the desired resolution for the SLS process and the dimensions of the printing chamber.

According to the aforementioned parameters, an initial computation has promptly demonstrated the unfeasibility of directly focusing the outgoing beam from the modules by means of a single lens (Figure 3.2). This is due to the constraint imposed by the distance between the processing head and the printing plane, which demands a focal length exceeding 120 mm, and the source characteristics in terms of collimated beam size and  $M^2$ .

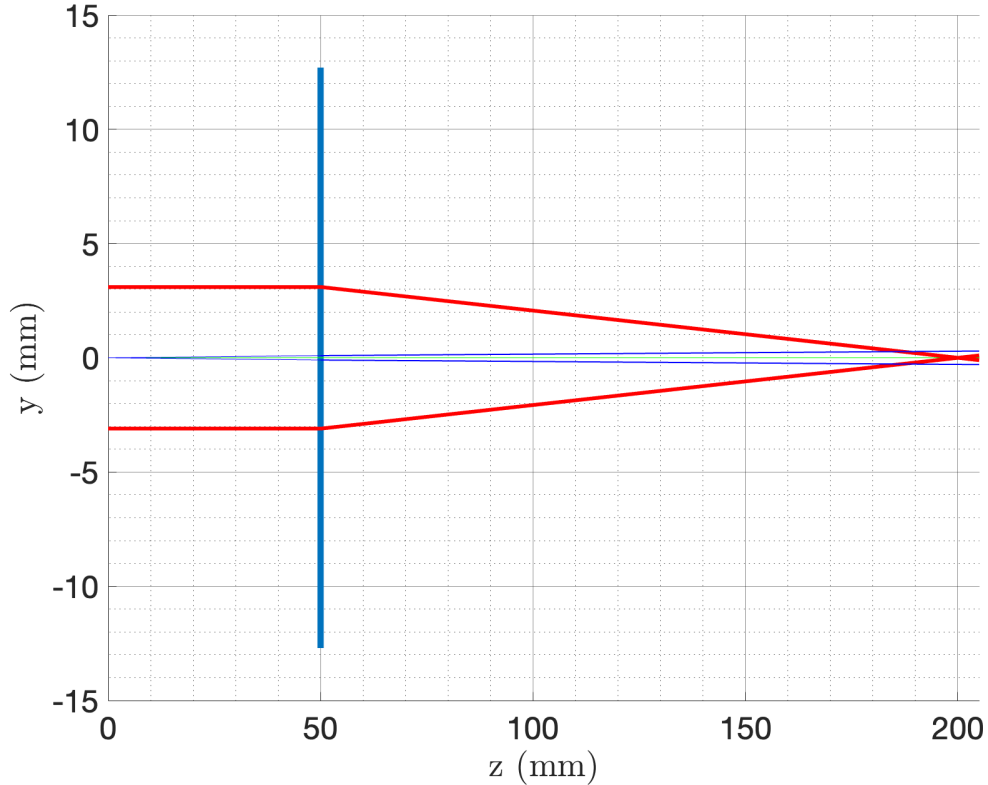


Figure 3.2: Ray tracing scheme of the configuration with one single focusing lens.

The spot diameter obtained using a single focusing lens of 150 mm focal length measures  $358\ \mu\text{m}$  along the SA and  $628\ \mu\text{m}$  along the FA. These values are deemed entirely unacceptable for SLS application since they exceed the limits required to guarantee adequate print resolution.

### 3.3.1 Galilean beam expander

Following this result, the need to opt for a more complex optical system became evident. The solution considered was the insertion of a Galilean beam expander to increase the size of the beam before the focusing lens, in order to obtain a smaller focused spot.

A beam expander is a device designed to enlarge the diameter of a laser beam while preserving the beam quality. Considering that the BPP is a constant factor, its primary purpose is to reduce the divergence angle of the beam by increasing the beam waist radius.

A typical Galilean beam expander uses a concave lens and a convex lens, as illustrated in 3.3.

The concave lens causes light rays to spread out as they pass through it while the convex

lens is used to recollimate the beam [9].

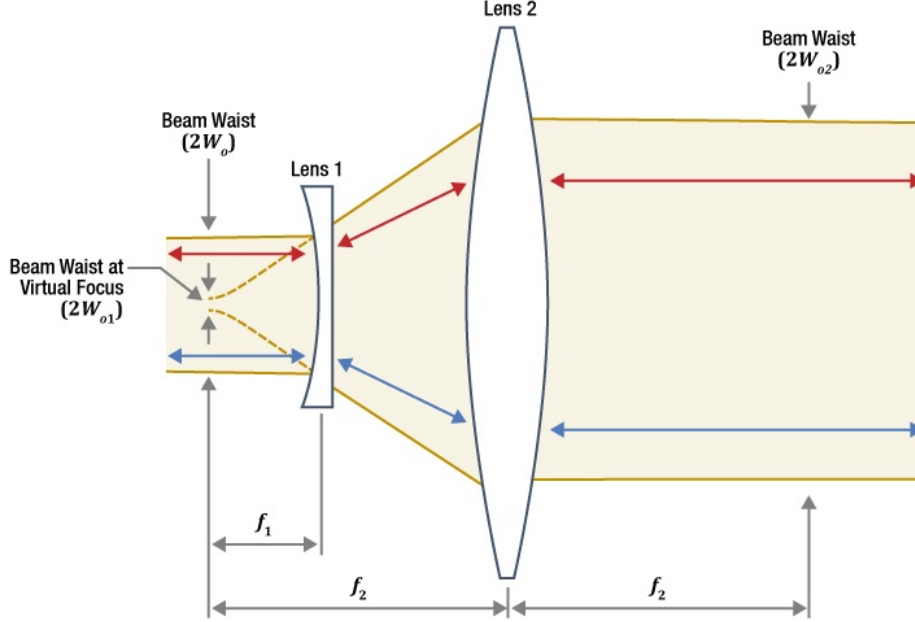


Figure 3.3: Galilean beam expander.

In order for the beam expander to function properly and produce a perfectly collimated output beam, it is necessary for these two lenses to be positioned at a distance equal to  $f_2 - f_1$ , where  $f_1$  is the focal length of the concave lens and  $f_2$  is the focal length of the convex lens.

The magnification of the beam expander is given by the ratio between the two focal lengths:

$$M_{12} = \frac{f_2}{f_1} \quad (3.5)$$

The advantages of using this type of beam expander are essentially two. The first is the absence of a real focus of the beam, which would result in high power density zones inside the optical path. The second is the possibility of compact size due to the presence of the concave lens with a negative focal length, which, for the same focal length and magnification ratio, requires an optical path that is half the length needed for a convex lens.

For the application in question, considering the initial size of the beam of  $2.15 \text{ mm} \times 3.1 \text{ mm}$ , a magnification ratio  $M_{12} = 5$  was chosen. This value was deemed the right compromise to stay within the clear aperture of the lenses and keep the dimensions of the processing head contained (Figure 3.4).

To obtain this magnification ratio the focal lengths of the lenses had been fixed at  $f_1 = -30 \text{ mm}$  and  $f_2 = 150 \text{ mm}$ . The collimated beam resulting from the expansion presents

a 10.8 mm spot diameter on the SA and 15.54 mm on the FA

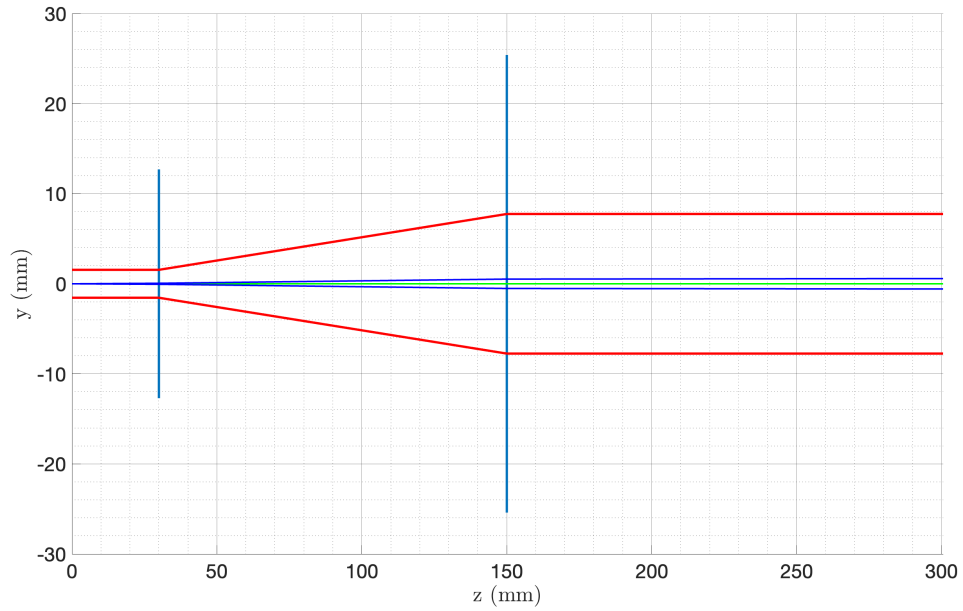


Figure 3.4: Ray tracing scheme of the collimation through the beam expander.

### 3.3.2 Design of the focusing length

As already mentioned, the required specifications for the final spot on the print plane taken into account for the design are from 100  $\mu\text{m}$  to 200  $\mu\text{m}$  in diameter at least at 120 mm from the processing head.

Considering the need to insert an output window to completely seal the device and preserve it from external contaminations, a focal length of 150 mm has been chosen for the focusing lens, in order to have a margin with respect to the project limits.

The focusing lens had the possibility to be located just after the beam expander to contain dimensions, since the beam outgoing from the beam expander is collimated (Figure 3.5). The final spot obtained with this configuration results to have a diameter of 114.9  $\mu\text{m}$  on the SA and of 124  $\mu\text{m}$  on the FA.

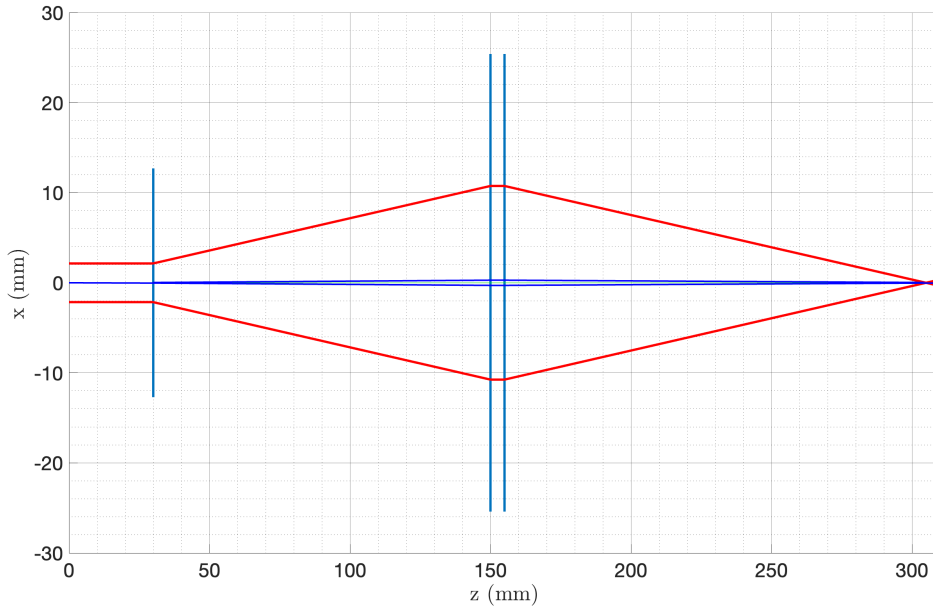


Figure 3.5: Ray tracing scheme of the system with beam expander and focusing lens.

This result lead to a maximum intensity on the target of  $1.07 \text{ MW cm}^{-2}$ , calculated as:

$$I_{\text{MAX}} = \frac{P}{\pi w_{\text{foc}}^2} \quad (3.6)$$

It is important to emphasize that for the intensity calculation, the relationship for ideal Gaussian beams has not been used due to the value of  $M^2$  of the modules. In fact, it is more careful not to take into account the typical multiplicative factor of the intensity of

Gaussian beams, reported in Equation 3.7.

$$I_{\text{MAX}} = \frac{2P}{\pi w_{\text{foc}}^2} \quad (3.7)$$



## Chapter 4

# Thermal analysis

The thermal characterization of the lenses was a crucial aspect of the design phase, as it ensured the optimal operation of the system and averted potential damage to the optics that could otherwise compromise the entire system.

Moreover, the thermal analysis was necessary to evaluate the sensitivity of the system to the thermal focal shift phenomenon, particularly critical when operating with focused laser beams.

This activity was accomplished by conducting a simulation phase utilizing COMSOL finite element analysis software, along with a series of laboratory experiments that served to validate the simulation outcomes.

However, the experimental setup available in the Alite laboratories did not allow a satisfactory measurement of the heating of the lenses as the power of the 30 W blue multi-emitter module used for all the laboratory experiments, waiting for the availability of the 60 W modules, was not sufficient to obtain a heating curve accurate enough to be used as a reference to obtain a model for the simulations.

A different setup was used to build up the model. The latter involved the use of an n-Light 1 kW infrared ( $\lambda_0 = 1070$  nm) laser and a lens made in fused silica with an anti-reflection coating suitable for this wavelength. This setup was first simulated in order to adjust all the simulation parameters and ensure that the results obtained were consistent with the measured data and subsequently the simulation setup has been modified with parameters suitable to simulate the behavior of the lenses with the blue beam.

## 4.1 Simulation of the Infrared setup

The simulated system consists of a Gaussian beam with an optical power of 1 kW, incident on a collimating lens with a beam radius  $w_0 = 2.5$  mm, identical to the beam exiting the n-Light laser and the lens' CAD downloaded from Thorlabs website (Figure 4.1).

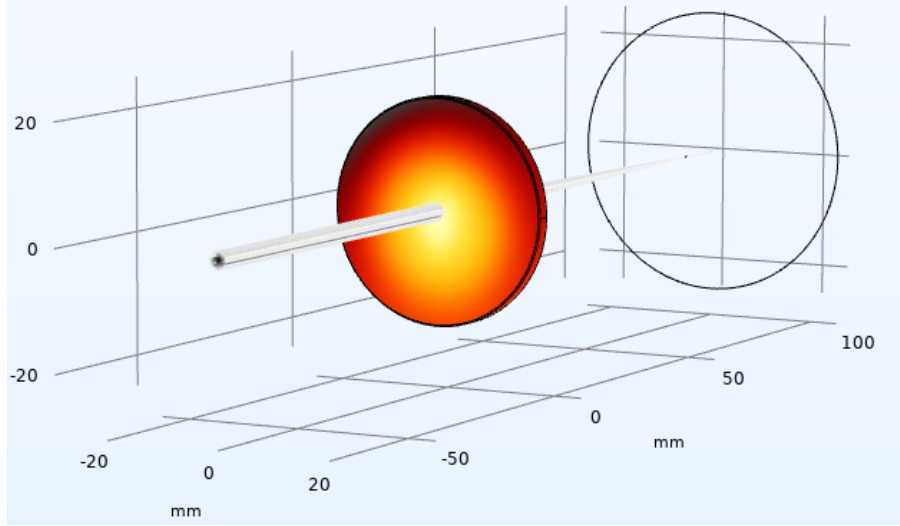


Figure 4.1: COMSOL simulation setup.

The COMSOL's physics modules utilized in this simulation activity are:

- *Geometrical Optics* to simulate the Gaussian beams and refractive phenomena within the lens with corresponding ray tracing of the beam (which was negligible for this analysis).
- *Heat Transfer in Solids* to simulate the thermal heating effects caused by the lens absorbing the optical power, as well as cooling effects due to convective heat flux with the surrounding air.

The parameters which have been taken into account for the simulation of the lens heating are:

- $h$ , the heat transfer coefficient of the convective flux with the surrounding air. The value that has been considered for this coefficient is  $h = 10 \text{ W m}^{-2} \text{ K}^{-1}$ .
- $\alpha$ , the absorption coefficient of the fused silica for the heat transfer analysis. After several researches in literature the value for this coefficient was set to  $\alpha = 10^{-4} \text{ cm}^{-1}$  [10].
- $n_i$ , the imaginary part of the refractive index of fused silica, calculated from the absorption coefficient *alpha* above mentioned as

$$n_i = \frac{\lambda_0 \alpha}{4\pi} \quad (4.1)$$

The simulation involved exposing the lens to the beam for a duration of 120 seconds and subsequently cooling it for an interval of 110 seconds. The simulation generated a plot depicting the temperature evolution over time (Figure 4.2) and a thermal map of the lens at the moment of maximum heating (Figure 4.3).

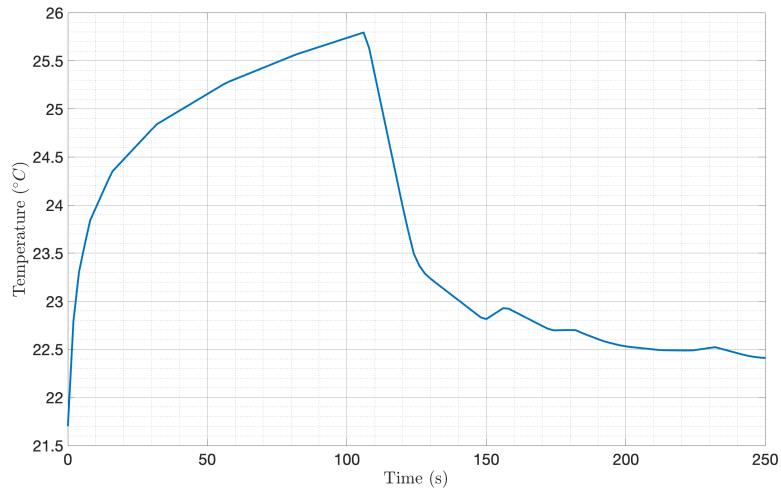


Figure 4.2: Heating of the lens with 1 kW infrared radiation simulated in COMSOL.

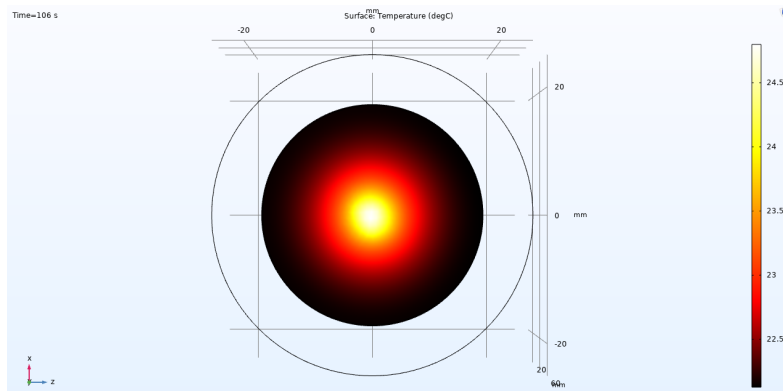


Figure 4.3: Heat map of the lens with 1 kW infrared radiation simulated in COMSOL.

The maximum temperature is reached in the center of the lens and it does not exceed 26 °C.

## 4.2 Experimental measurement on the Infrared setup

The measurements on the setup arranged in the laboratory were taken with a FLIR thermal camera positioned in the vicinity of the optical path so as to directly capture the surface of the lens (Figure 4.4).

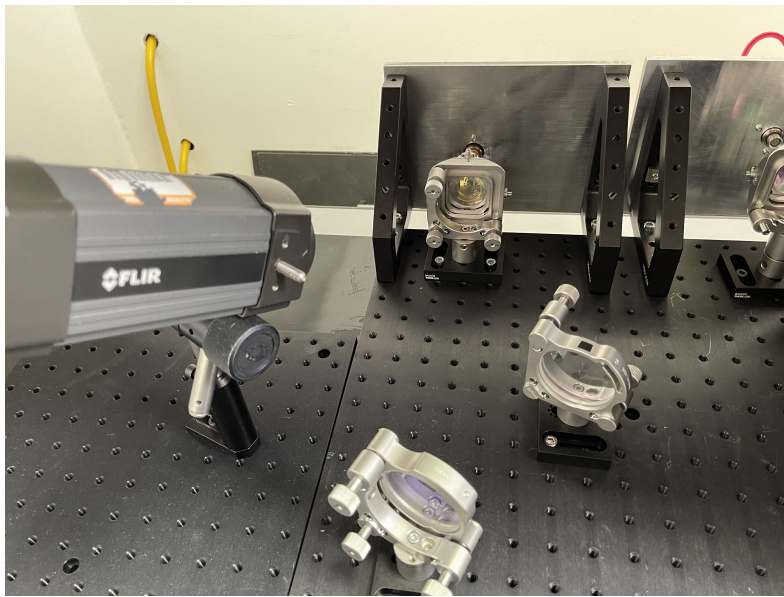


Figure 4.4: Experimental setup for temperature measurements on the infrared setup.

Various acquisitions were made with exposure times and cooling as similar as possible to those simulated on COMSOL. The best result of the acquisitions obtained from the experimental activity is reported below in Figure 4.5.

Starting from a room temperature of  $21.7^{\circ}\text{C}$ , the lens traversed with an optical power of  $1\text{ kW}$  for  $110\text{ s}$  does not exceed the temperature of  $25.5^{\circ}\text{C}$ , measured in the point of maximum heating (Figure 4.5).

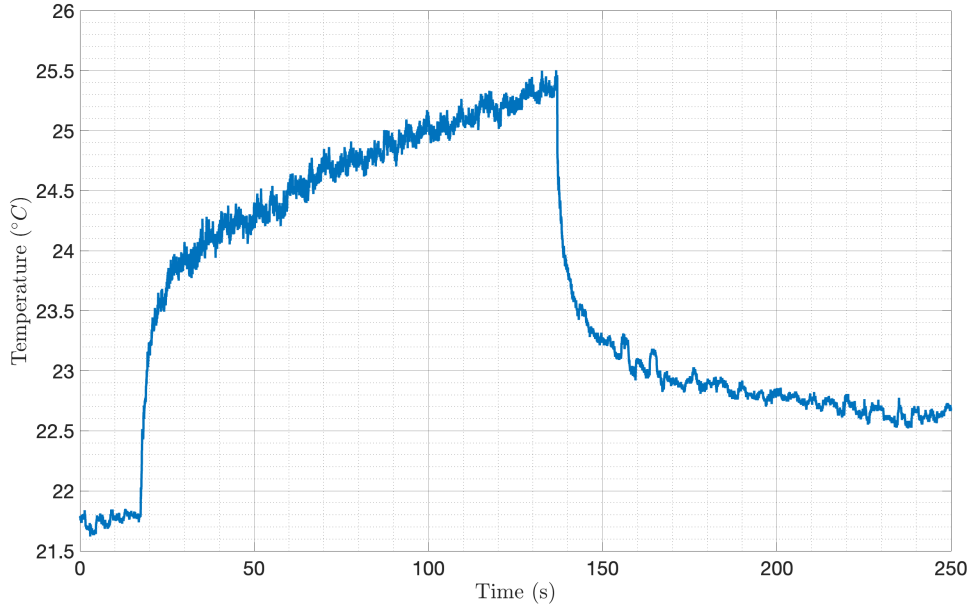


Figure 4.5: Trend of the temperature detected on the center of lens by the FLIR thermal imaging camera.

The experimental measurement demonstrate a behavior similar to the simulated one, thus it is possible to consider the model used in the simulations and the results obtained reliable.

### 4.3 Simulation of the Blue setup

Given the positive results obtained from the simulations of the IR setup, the same model was reused to make a prediction of the heating of the optics present in the head exposed to blue radiation.

The parameters were adapted to the characteristics of the blue beam by changing the wavelength value from  $\lambda_0 = 1070$  nm to  $\lambda_0 = 445$  nm, the absorption coefficient from  $\alpha = 10^{-4} \text{ cm}^{-1}$  to  $\alpha = 10^{-3} \text{ cm}^{-1}$ , setting the optical power to 120 W and the diameter of the incident beam to 2.6 mm, which is an average between the dimensions of the beam along the FA and the SA.

The lens' heating has been simulated for 600 seconds to observe the steady state behavior of the temperature.

However, it's important to point out that the lens heating is strongly influenced by characteristics that are closely related to the specific lens used such as the center thickness, the purity of the fused silica, the scratch-dig and ARC specifications and the degree of cleaning of the lens surface.

In these simulations, only the first plano-convex lens was taken into account, as it is the most critical element since it is the one on which the highest power density falls, being exposed to a collimated beam of 120 W of optical power on a spot of  $2.15 \text{ mm} \times 3.1 \text{ mm}$  and, therefore, it is subject to the greatest local heating, however reaching a steady state temperature lower than  $23.5 \text{ }^\circ\text{C}$  (Figure 4.6) in the center of the lens (Figure 4.7).

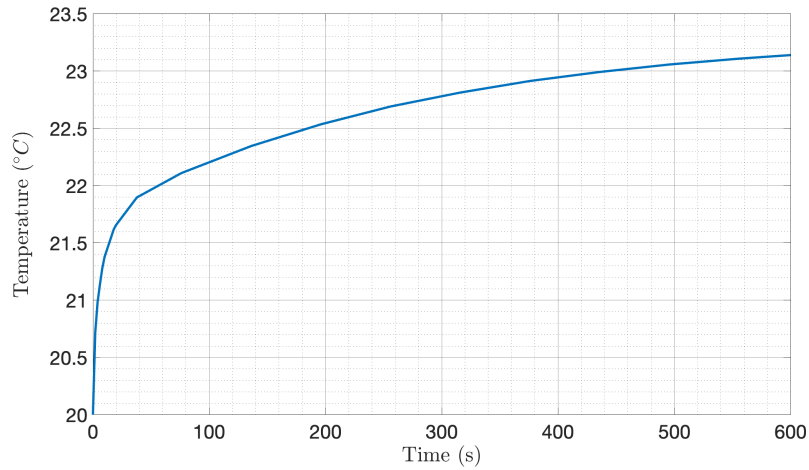


Figure 4.6: Heating of the lens with 1 kW infrared radiation simulated in COMSOL.

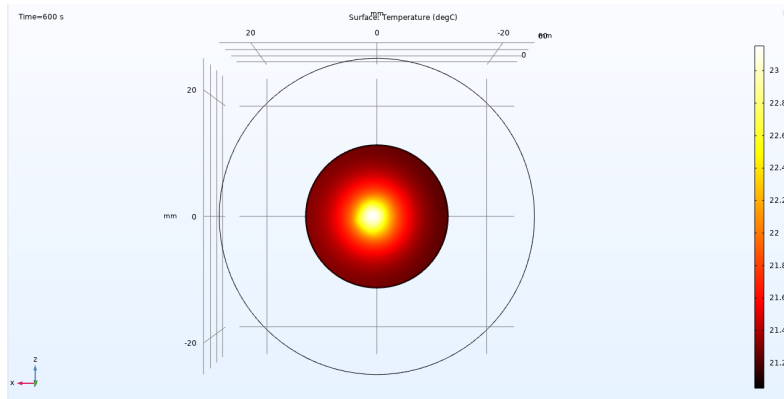


Figure 4.7: Heat map of the lens with 120 W blue radiation simulated in COMSOL.

## 4.4 Thermally induced focal shift analysis

The last step of the thermal analysis was the evaluation of the thermal focal shift induced as a consequence of the lens heating.

The thermal focal shift is a phenomena which comes out when an high power laser beam passes through an optical component: the thermal expansion as well as the variation of the refractive index of the optical materials can change the lens' focus [11].

In the system under analysis this effect could manifest itself in the variation of the focal length of the plano-concave defocusing lens. This could lead to a variation of the magnification ratio of the beam expander and to a consequent modification of the shape of the focused spot and its position along the optical axis. Since after this lens the beam diameter is considerably large, there is no localized accumulation of power such that thermal induced focal shift phenomena can occur on plano-convex lenses placed after the first lens.

Anyway, the simulations carried out show that the plano-concave lens is subject to minimal heating which is negligible for the purpose of evaluating the presence of thermally induced focal shift.



## Chapter 5

# Advanced ray tracing

The final stage of simulation of the optical system to be integrated into the processing head was carried out using the Zemax OpticStudio ray tracing software to obtain more accurate results compared to the simple simulations with Gaussian beams carried out in the initial phase.

### 5.1 Source simulation

Initially, the simulation process involved generating a source with beam characteristics that closely resemble those of the commercial modules illustrated in Figure 5.1.

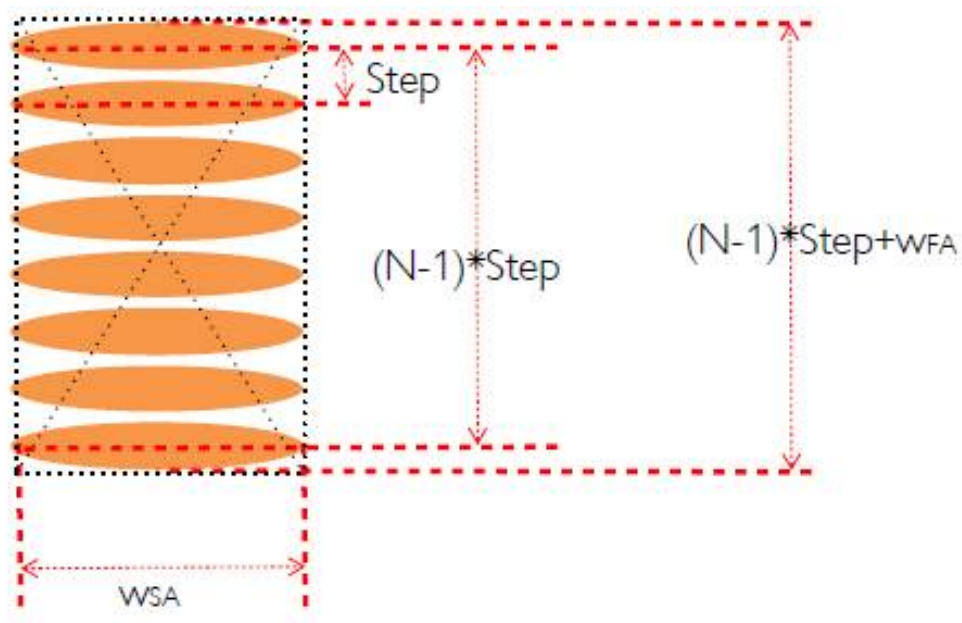


Figure 5.1: Output characteristic of the multi-emitters modules.

For this purpose, two *Source Diode* sources were utilized and superimposed to simulate a spectral combination. Each of these sources comprised of 8 stacked virtual diodes, vertically spaced by a *Step* parameter of 0.4 mm and with divergence  $\theta_{SA} = 1.87$  mrad and  $\theta_{FA} = 1.93$  mrad.

Since each diode is simulated as a point source, the *Astigmatism* parameter of the *Source Diode* (Figure 5.2) has been calculated as explained in Equation 5.1 in order to obtain the simulated beam waist diameter on the SA  $w_{SA} = 2.15$  mm and the source has been shifted by 69.9 mm in the negative z-axis direction in such a way as to obtain a FA beam waist diameter  $w_{FA} = 0.27$  mm at position  $z = 0$ .

$$Astigmatism = \frac{w_{SA}}{2 \tan \theta_{SA}} = 574.9 \text{ mm} \quad (5.1)$$

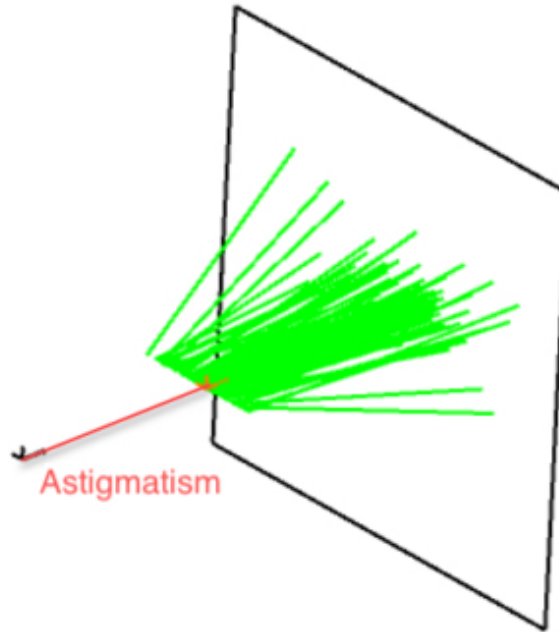


Figure 5.2: Graphical explanation of the Astigmatism parameter from OpticStudio' s help guide.

The field distribution of the simulated source obtained with the parameters just explained is shown in the Figure 5.3 and the result of the superposition of two sources is represented in Figure 5.4.

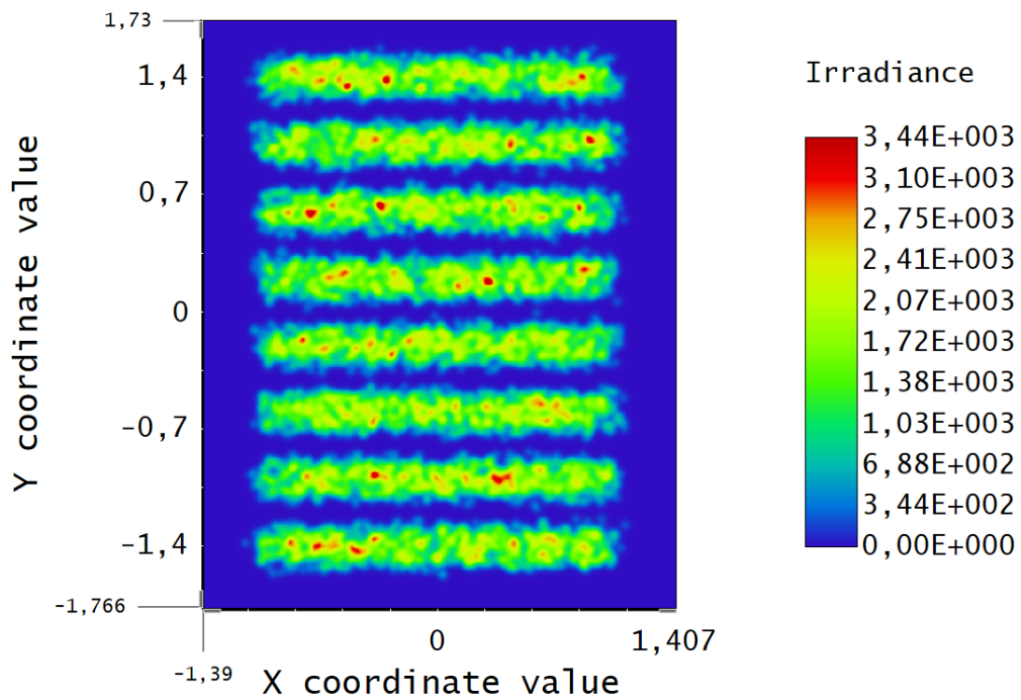


Figure 5.3: Spot diagram of a simulated source.

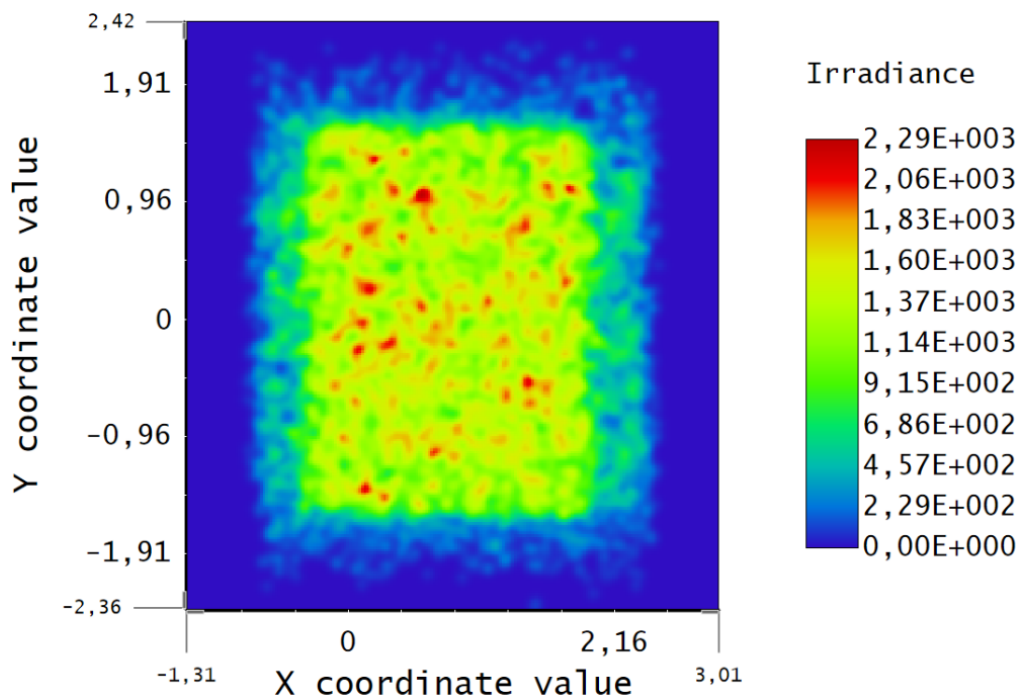


Figure 5.4: Spot diagram of the superposition of two simulated sources spectrally combined.

## 5.2 Simulation of the optical system

With regard to the simulation of the lens sequence, the CAD files of the lenses chosen for the experimental phase were downloaded from the Thorlabs website and loaded into OpticStudio. The selected lenses are:

- LA4904-A: plano-convex lens with focal length  $f = 150$  mm and 50.8 mm diameter.
- LC4252-A: plano-concave lens with focal length of  $f = -30$  mm and 25.4 mm diameter.

The lenses were arranged using OpticStudio's non-sequential editor interface. For positioning along the optical axis, the focal lengths of the selected lenses were used as reference.

The diagram of the lens arrangement and the simulated rays from OpticStudio's ray tracing are shown in Figure 5.5.

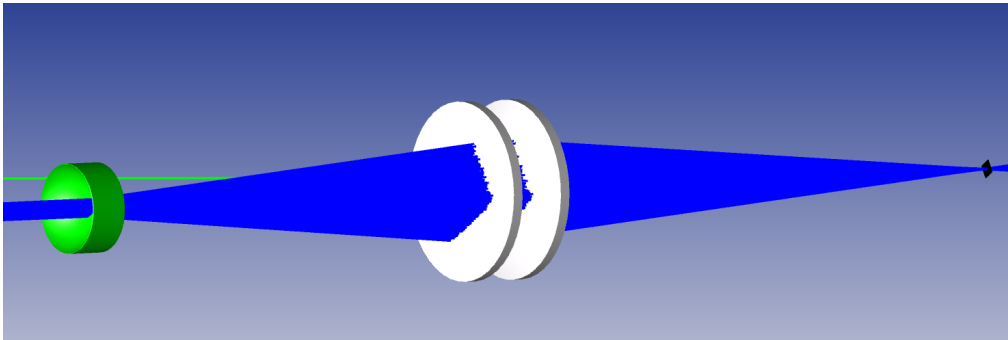


Figure 5.5: Lenses sequence in OpticStudio 3D Non-Sequential Component view with traced rays.

### 5.3 Analysis of the simulation results

Some *Detector rectangle* objects were placed along the optical axis in order to analyze the evolution of the beam through lenses and to calculate the spot size.

This made it possible to calculate the size of the collimated beam exiting from the beam expander (Figure 5.6), which is equal to 10.4 mm on the FA and 8.1 mm on the SA, intended as the  $1/e^2$  beam diameter.

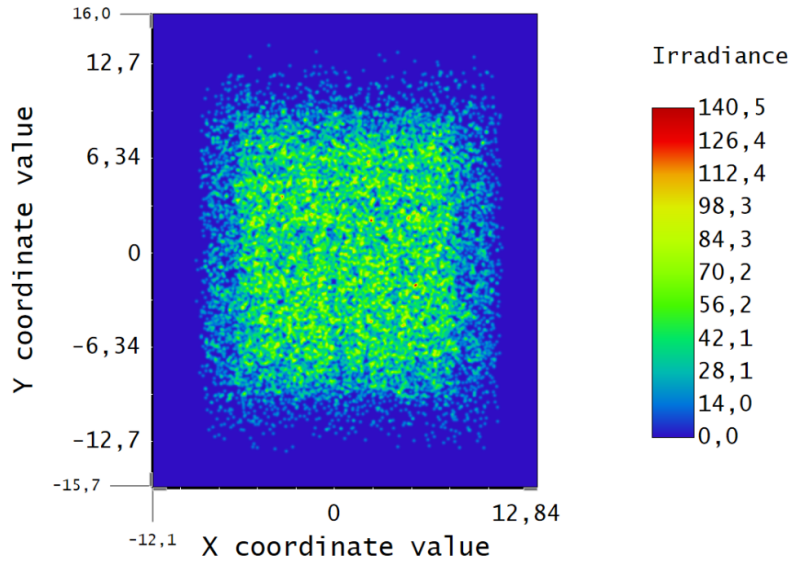


Figure 5.6: Spot diagram of the collimated beam exiting the beam expander.

Following the beam expander, the focusing lens was positioned immediately after the collimation lens, leaving enough space for the dimensions not to overlap and allowing a detector to be inserted between the two lenses to visualize the spot.

The spot size at the focus of the 150mm focusing lens has diameter on the detector equal to 116  $\mu\text{m}$  on the SA and 90  $\mu\text{m}$  on the FA with the irradiance profile depicted in Figure 5.7.

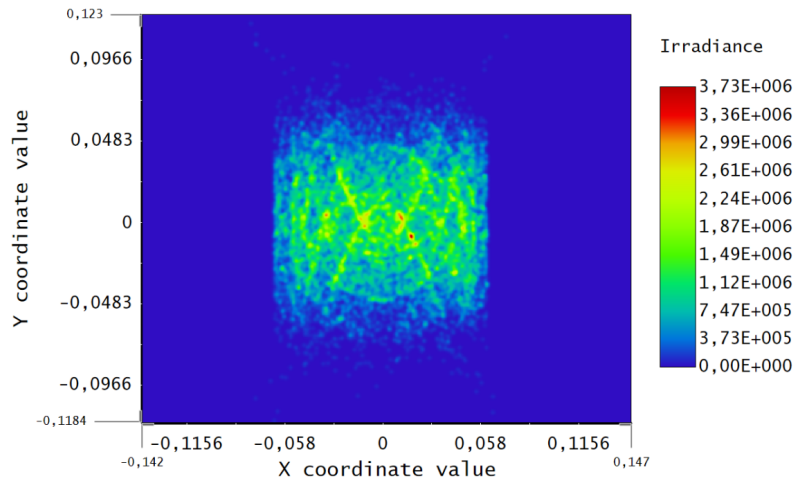


Figure 5.7: Final spot detected at the focus of the focusing lens.

The dimensions predicted by this simulation activity were found to be completely in line with the required specifications and have served as validation for the optical system parameters defined during the first design phase performed with Gaussian beams.

Clearly, the results of simulations carried out with OpticStudio differ significantly from simulations with Gaussian beams in terms of beam profile and, consequently, peak irradiance. In fact, the one of the beam emitted by the multi-emitter modules is distinctly far from being a Gaussian distribution and also the shape is not circular but more similar to a rectangular profile.

This significantly impacts the peak intensity value predicted by OpticStudio, which is noticeably higher than that calculated from simulations with Gaussian beams, despite the simulated final spot sizes being comparable. The peak irradiance on the print plane should be around  $3.73 \text{ MW cm}^{-2}$ .

## Chapter 6

# Experimental setup

As a result of the satisfactory outcomes obtained from the OpticStudio simulations of the system designed during the design phase, the required materials were purchased to construct a benchtop prototype of the processing head for performing experimental measurements of the parameters of the final spot.

The prototype was fabricated utilizing a Thorlabs cage system (Figure 6.1), which was instrumental in preserving the inter-lens alignment and creating a sturdy and convenient apparatus for conducting all measurements.



Figure 6.1: Example of Thorlabs' cage system.

In order to achieve precise control over the orientation angles and positioning of the

lens along the optical axis, the decision was made to opt for 3-axis kinematic mounts as the lens holders of choice (Figure 6.2).



Figure 6.2: Thorlabs 3-axis kinematic lens mounts.

The chosen optics consist of two plano-convex lenses having a focal length of 150 mm and one plano-concave lens with a focal length of  $-30$  mm. UV fused silica lenses were preferred for the prototype since it is a high purity glass material that has excellent transmission properties and a low coefficient of thermal expansion, which makes it highly resistant to thermal shock.

## 6.1 Beam expander assembly and collimation

The assembly process for the head was divided into two parts, with the initial block consisting of a beam expander comprised of a plano-concave lens followed by one of the two plano-convex lenses.

Owing to the unavailability of the 60 W modules, a 30 W commercial multi-emitter module was utilized for the measurements, which had an output beam characteristic identical to that of the 60 W modules.

Since this module was designed for fiber output rather than air output, it was not secured to the cage system. To extract the collimated beam from the multi-emitter, two right-angle prism mirrors were utilized (Figure 6.3) and the cage system with the lenses was aligned to the beam using precision adjustment on the optical table.

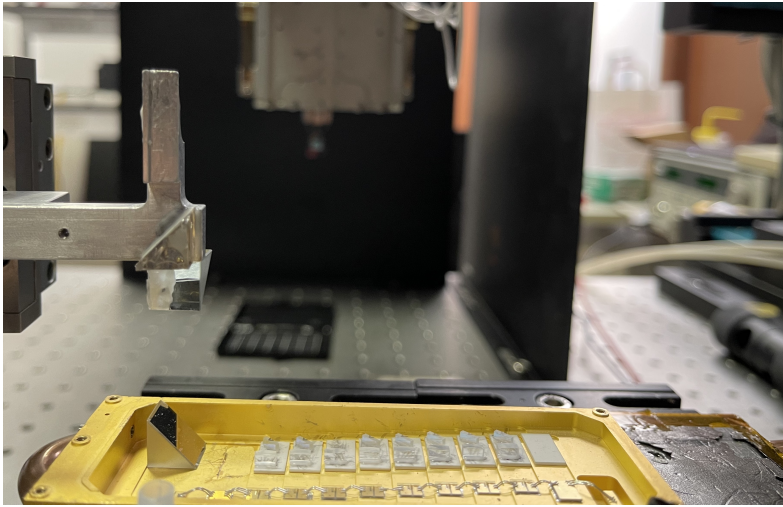


Figure 6.3: Multi-emitter module arranged for air output.

Starting from a collimated beam, the only critical aspect in assembling the beam expander was positioning the two lenses so that their principal planes were at a distance  $d$  equal to the sum of their EFL (Figure 6.4).

$$d = f_2 + f_1 = 150 \text{ mm} + (-30 \text{ mm}) = 120 \text{ mm} \quad (6.1)$$

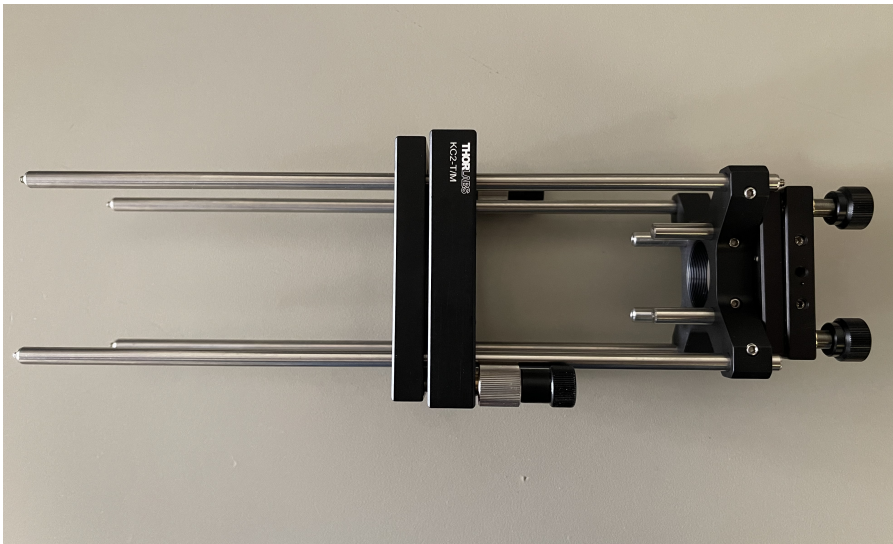


Figure 6.4: Beam expander assembled with cage system.

This was achieved experimentally by using the precision adjustment of the lens mount to control the position of the 150 mm lens along the optical axis after an initial rough positioning. The size of the output beam spot was measured using a motorized linear stage, ensuring that it remained constant over long distances.

The precision adjustments have also been used to attain precise alignment between the two lenses, thus minimizing distortions in the output beam and ensuring optimal performance.

## 6.2 Assembly of the focusing lens

Upon collimating the output beam from the beam expander, the lens mount comprising the second lens with EFL of 150 mm was installed onto the cage system for beam focusing (Figure 6.5).

Due to its placement in front of a collimated beam, the positioning of this element along the optical axis was not deemed critical. Nevertheless, the utilization of precision adjustments was pivotal in ensuring optimal alignment of the lens, thereby preventing unwanted distortions or reflections in the focal point.

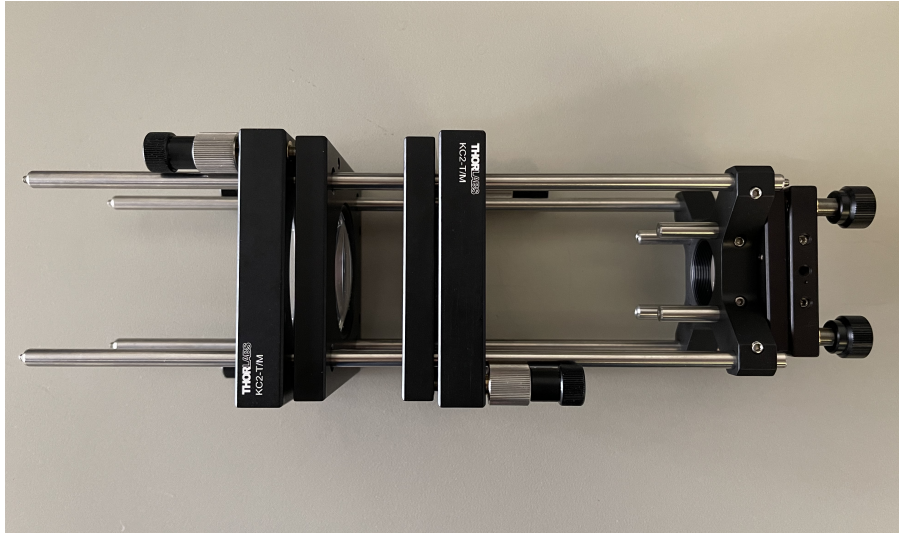


Figure 6.5: Processing head fully assembled with cage system.

The focus was detected by positioning a Thorlabs CMOS camera (Figure 6.6) on the motorized linear stage (Figure 6.7) about 150 mm away from the focusing lens and moving it along the optical axis in 20  $\mu\text{m}$  steps until the position where the displayed spot had the smallest size was identified.



Figure 6.6: CMOS camera used for the spot measurements (Thorlabs DCC3260C).

It is imperative to highlight that the placement of the camera at the beam focus, where an extremely high power density exists, is a non-trivial task. As a result, two reflective ND4 filters were inserted between the multi-emitter module output and the head prototype to diminish by eight orders of magnitude the beam power incident on the camera.

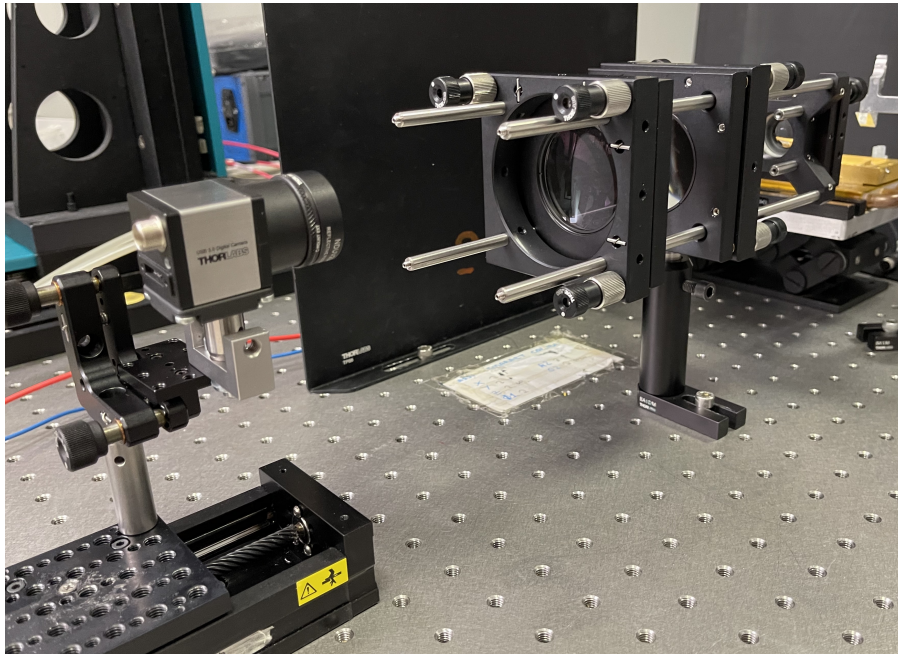


Figure 6.7: System used to detect the focused spot.

Regrettably, the filters' presence led to the camera sensor picking up disturbances that deteriorated the quality of the captured images and resulted in a slight distortion of the focused spot. However, this did not hinder a valid measurement of the focused spot

achieved.

### 6.3 Measurement of the spot size

The measurements of the spot were conducted utilizing the sensor pixels with a square shape of  $5.86\ \mu\text{m}$  per side as specified in the datasheet. However, due to the requisite significant attenuation of the beam by the filters to prevent damage to the camera, the full dynamic range of the CMOS sensor could not be employed, precluding measurement of the spot at the point where its intensity is  $1/e^2$  (13.5%) of its maximum. Instead, the spot was determined by pixel counting of the acquired image, subject to an uncertainty of  $\pm 1\ px$ .

The resulting image from the measurement is shown in Figure 6.8 and the measured spot has dimensions  $23 \times 18\ px$  which converted means a diameter of  $134.8\ \mu\text{m}$  on the SA and  $105.5\ \mu\text{m}$  on the FA.

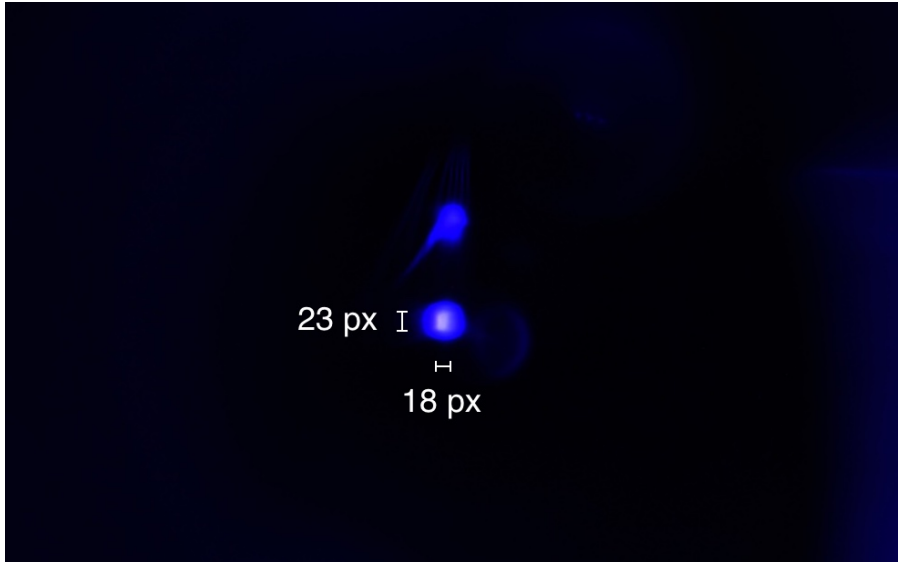


Figure 6.8: Image of the focused spot captured with Thorlabs CMOS camera.

Taking into account the high value of the  $M^2$  of the modules used and assuming the use of two 60W modules spectrally combined without losses, it is possible to estimate the peak intensity value as:

$$I = \frac{P}{\pi w_{FA} w_{SA}} = 2.69\ \text{MW cm}^{-2} \quad (6.2)$$

The fact that the measured peak irradiance is lower than the one predicted by the simulations in OpticStudio can be justified by alignment errors of the optics during the assembly phase due to tolerances of the cage elements and the lack of an appropriate vision system to monitor the positioning and orientation of all lenses with the necessary sensitivity.

Optical systems are sensitive to even small misalignments or deviations from the expected geometry, which can significantly affect the performance of the system, such as the spot size, introducing distortion phenomena.

Therefore, having a larger spot size due to distortions necessarily results in a reduction of the peak intensity value.

## 6.4 Measurement of the divergence

The experimental measurement of beam divergence involved the use of the motorized linear stage to move the CMOS camera along the optical axis. Subsequently, the camera captured an image of the spot in focus, followed by a second image of the spot located 10 mm away from the focal point.

The spot captured at this point has dimensions of  $161 \times 212 \text{ px}$ , meaning a diameter of  $943.5 \mu\text{m}$  on the SA and  $1242.3 \mu\text{m}$  on the FA (Figure 6.9).

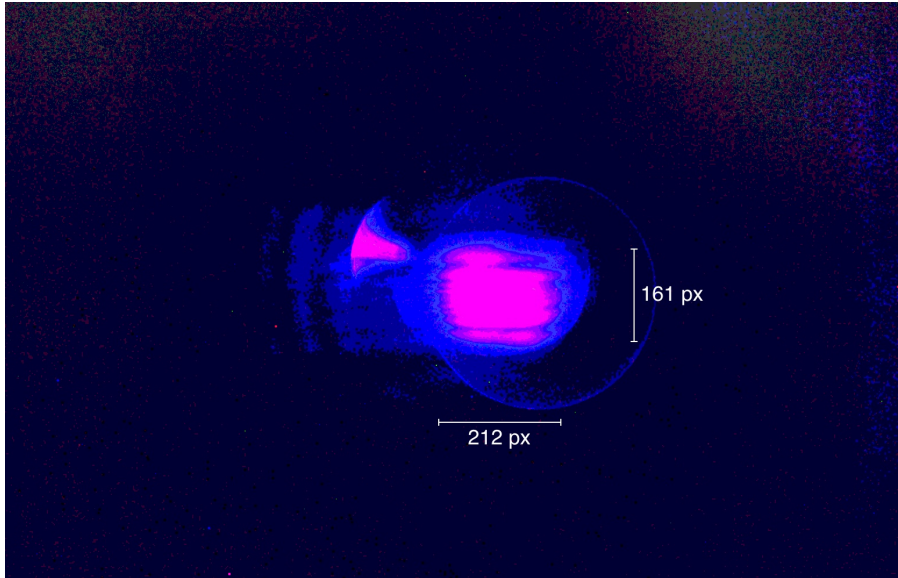


Figure 6.9: Image of the spot captured at 10 mm away from the focal point with Thorlabs CMOS camera.

A resulting divergence of the beam  $\theta_{\text{SA}} = 80.6 \text{ mrad}$  and  $\theta_{\text{FA}} = 113.2 \text{ mrad}$  has been calculated considering the relationship in Equation 6.3.

$$\theta = \arctan \left( \frac{w_{10\text{mm}} - w_{\text{foc}}}{10 \text{ mm}} \right) \quad (6.3)$$

## **6.5 Measurement of the thermally induced focal shift**

Due to the limits imposed by the damage threshold of the CMOS camera used for the spot measurements, it was not possible to carry out the experimental measurement of the thermally induced focal shift.

In fact, to carry out this measurement, it would have been necessary to turn on the multi-emitter module at full power for several minutes and wait for the lenses to heat up. This was not possible for two reasons: firstly, there were not enough ND filters available to lower the beam power to a value that would allow the measurement of the spot and the focus position with the CMOS camera.

Furthermore this type of filter can be positioned exclusively in front of a collimated beam and therefore it would not have been possible to perform the measurement by positioning them after the beam expander to allow at least the first lens to heat up due to the dimensions of the beam collimated by the beam expander, which would have been greater than the diameter of the available filters.

However, this measurements could not be performed with the available multi-emitter module since the heating of the lens with a 30 W beam can be considered totally negligible.

# Chapter 7

## Conclusions

The activities carried out in this thesis have made it possible to develop and create a fully functional prototype of a processing head potentially capable for SLS of metal powders and polymers.

### 7.1 Results achieved

All experimental measurements confirmed the expected values from the simulations performed on the designed optical system. Ultimately, since the output characteristics of the 60 W modules (not yet available at the time of writing this chapter) will be identical to those of the 30 W module used for the measurements and the spectral combination of two modules does not worsen the BPP of the produced beam, it is quite accurate to expect a power of about 120 W, except for any losses due to module stabilization, on a slightly astigmatic spot measuring  $134.8\ \mu\text{m}$  on the SA and  $105.5\ \mu\text{m}$  on the FA with a peak irradiance of  $2.69\ \text{MW cm}^{-2}$ .

It is important to emphasize that these values could be further improved and the designed system could have better performance than those detected with a more accurate alignment of the lenses, which, however, would require additional instrumentation currently not available in the Alite laboratories.

## 7.2 Outlook

The future developments of the system designed in this thesis foresee the integration of the prototype on board the additive manufacturing machine for which it was designed.

Alite's mechanical department will take care of the integration of the developed optical system and the source into an integral block which can be moved by the mechanical slides for the phase of characterization of the prototype in working conditions which will be carried out by the customer.

Moreover, the sensors to be integrated inside the processing head for monitoring operation and detecting any problems due to misalignments are in the planning stage. Specifically:

- Back-scattering sensors are being developed to detect any scattering phenomena due to the presence of deposits such as dirt, fumes or processing waste, on the protection window that will be placed at the optical system output.
- Photodiodes will then be installed to detect any anomalous reflections due to damage or misalignment of the optical components present following mechanical or thermal stress.
- Temperature sensors to take trace of the ambient temperature and the optical devices' heating will be required to ensure that the device is always in optimal operating condition.
- Sensors to detect fluorescence phenomena from powders deposited on the printing plane could be taken into consideration to obtain information on temperature locally induced in the focal plane and adjust the printing parameters accordingly.

Developments on the front of the laser source used, conceived as a modular system for power scaling, provide for the possibility to obtain a combination of four multi-emitter modules resorting to a further step of spatial combination of two spectrally combined sources, to obtain a total power of over 200 W.

This type of combination would lead to a collimated beam consisting of the juxtaposition of two beams resulting from the spectral combination with characteristics identical to those analyzed in chapter 5 with an expected field profile similar to that shown in Figure 7.1.

For the manipulation of this beam through the optical system designed for the processing head, the effectiveness of a solution is being evaluated which sees the use of two axicon lenses in addition to the lenses of the optical system already described.

An axicon (Figure 7.2) is a conical prism. Unlike a converging lens which is designed to focus a light source to a single point on the optical axis, an axicon uses interference to create a focal line along the optical axis [12].

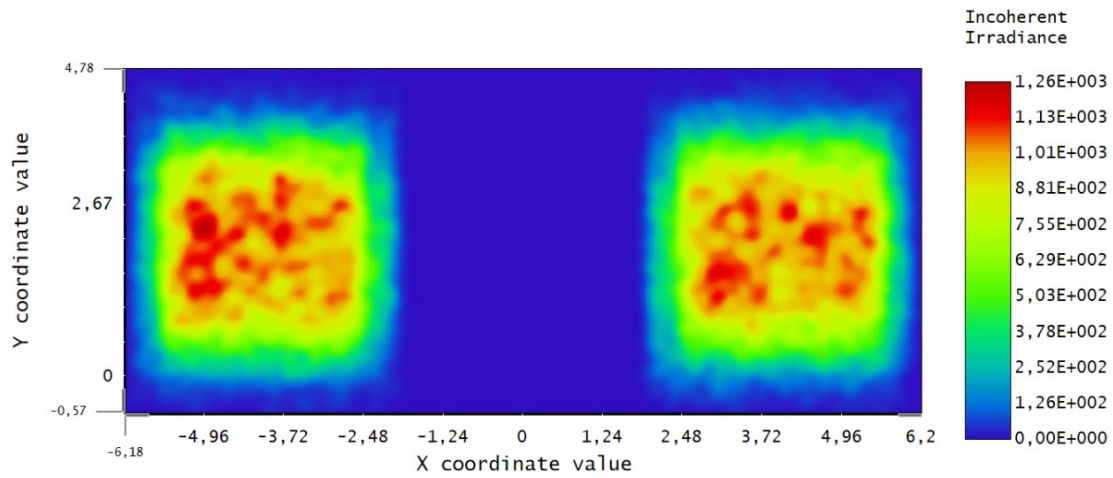


Figure 7.1: Spot of the collimated beam obtained from the spatial combination of two spectral combined source (four modules in total).

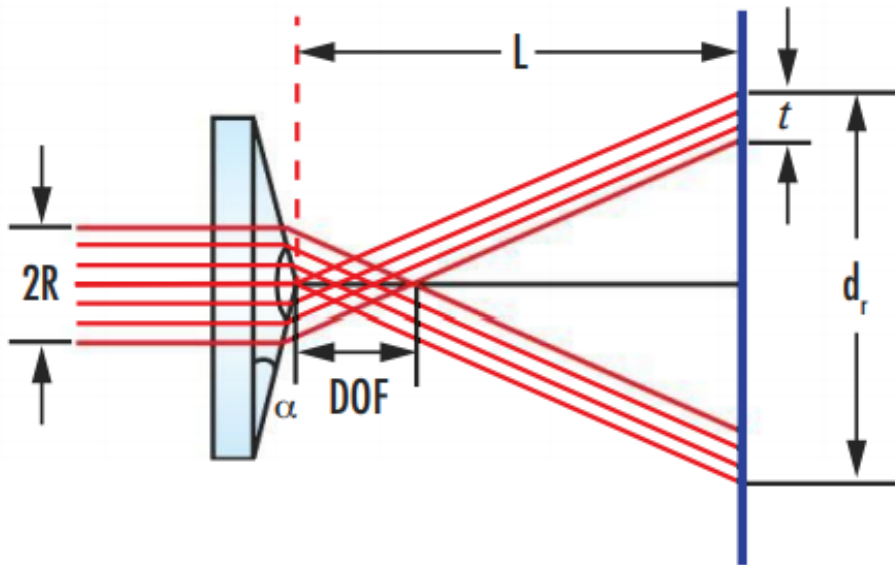


Figure 7.2: Schematic of an axicon lens' working principle.

Reversing the usual operating principle of an axicon lens, the potential utility of these specific lenses in this type of application is that of being able to superimpose the two beams that are separated at the source output.



# Bibliography

- [1] “Additive manufacturing, general principles, fundamentals and vocabulary,” p. 14, ASTM, 2021.
- [2] “Global laser technology market revenue analysis and forecast.” [www.acumenresearchandconsulting.com/](http://www.acumenresearchandconsulting.com/).
- [3] “Laser technology market size - global industry, share, analysis, trends and forecast 2022 - 2030,” p. 250, IEEE, 2022.
- [4] L. Li, “The advances and characteristics of high-power diode laser materials processing,” *Optics and Lasers in Engineering*, vol. 34, no. 4, pp. 231–253, 2000. Laser Material Processing.
- [5] Y. Xiong, C.-l. Jiang, A. Jamil, X. Liu, X. Liu, P. Modak, S. McDougall, and K. Boucke, “Advances in 976nm single emitter broad semiconductor diode lasers for 300w+fiber laser pump module applications,” in *HIGH-POWER DIODE LASER TECHNOLOGY XX* (M. Zediker and E. Zucker, eds.), vol. 11983 of *Proceedings of SPIE*, SPIE, 2022. Conference on High-Power Diode Laser Technology XX at SPIE LASE Conference, ELECTR NETWORK, JAN 22-FEB 28, 2022.
- [6] J. Piprek, “What limits the power conversion efficiency of gan-based lasers?,” in *PHYSICS AND SIMULATION OF OPTOELECTRONIC DEVICES XXV* (B. Witzigmann, M. Osinski, and Y. Arakawa, eds.), vol. 10098 of *Proceedings of SPIE*, SPIE, 2017. Conference on Physics and Simulation of Optoelectronic Devices XXV, San Francisco, CA, JAN 30-FEB 02, 2017.
- [7] K. Georgilas, R. H. U. Khan, and M. E. Kartal, “The influence of pulsed laser powder bed fusion process parameters on inconel 718 material properties,” *MATERIALS SCIENCE AND ENGINEERING A-STRUCTURAL MATERIALS PROPERTIES MICROSTRUCTURE AND PROCESSING*, vol. 769, JAN 2 2020.
- [8] “Lenses.” <https://www.rp-photonics.com/lenses.html>.
- [9] “Beam expander design comparison: Keplerian and galilean.” [https://www.thorlabs.us/newgrouppage9.cfm?objectgroup\\_id=14648](https://www.thorlabs.us/newgrouppage9.cfm?objectgroup_id=14648).
- [10] S. T. Yang, M. J. Matthews, S. Elhadji, D. Cooke, G. M. Guss, V. G. Draggoo, and P. J. Wegner, “Comparing the use of mid-infrared versus far-infrared lasers for mitigating damage growth on fused silica,” *APPLIED OPTICS*, vol. 49, pp. 2606–2616, MAY 10 2010.
- [11] “Thermally induced focal shift in high-power laser focusing systems.” <https://www.comsol.com/model/thermally-induced-focal-shift-in-high-power-laser-focusing-systems-19955>.

- [12] “An in-depth look at axicons.” <https://www.edmundoptics.com/knowledge-center/application-notes/lasers/an-in-depth-look-at-axicons/>.